

BACHELORARBEIT

Zur Erlangung des akademischen Grades Bachelor of Science

Monte Carlo Analysis Of The Acceptances In The $\pi^-\eta'$ And
 $\pi^-\eta$ Final States At COMPASS (CERN)



Ludwig-Maximilians-Universität München
Fakultät für Physik

vorgelegt von: **Maximilian Nikolaus Diefenbach**

geboren am: 30.03.1988 in München

Eingereicht am: 15.06.2011

Gutachter: Prof. Dr. Wolfgang Dünneweber

Abstract

The **CO**mmon **MU**on **PR**oton **AP**peratus for **S**tructure and **S**pectroscopy, short COMPASS is a fixed target experiment at CERN¹ in Geneva, Switzerland. As a two stage spectrometer, it aims to study the spectra and inner structure of hadrons and participates in the search for exotic mesons with quantum numbers J^{PC} that can not be obtained by quark-antiquark states. Former experiments give evidence for the existence of exotic resonances in the $\pi^-\eta'$ and the $\pi^-\eta$ final states[4][9]. For exact measurements of the quantum numbers of these exotics a partial wave analysis is required that relies on a good description of the acceptance of the detector response at COMPASS. In this thesis the acceptance as a function of various kinematic relevant variables is investigated through a Monte Carlo simulation of the $\pi^-\eta'$ and the $\pi^-\eta$ decay channels.

An event generator is used that simulates the diffractive excitation in the $p\pi^- \rightarrow pX$ process and lets the generated resonance X decay isotropically into $\pi^-\eta'$ or $\pi^-\eta$ with the η either disintegrating to two photons $\gamma\gamma$ or three pions $\pi^-\pi^+\pi^0$. The momentum transmission t' is exponentially distributed with a slope of 6 and starts at 0,1GeV². The mass of X is uniformly generated in the range of $[m_\pi + m_{\eta'/\eta}, 4\text{GeV}]$. The three-body decays in the respective decay channels are simulated with their experimental PDG weights. The simulated final states with three pions in the η' - and the η -channel and the final state with five pions in the η' -channel are put in COMGEANT and reconstructed with CORAL. The same generated final states are parallelly selected in a fast Monte Carlo program with a rudimental implementation of only the geometry of the RICH and the ECALs, where a photon energy higher than 1GeV and in ECAL2 higher than 4GeV is required. The acceptances for both the full Monte Carlo and the fast Monte Carlo simulation are studied and compared with each other.

In general the efficiency in the full Monte Carlo is always lower compared to the photon acceptance, since no charged particle detection is implemented in the fast Monte Carlo. As a function of the t' -distribution, the xy -distribution of the vertex position and the Dalitz plots the acceptances are flat in every observed decay channel, which is clearly in agreement of the two Monte Carlo simulations. The non-uniform acceptances as functions of generated resonance mass m_X , the z -distribution of the vertex position and the azimuthal angle φ_{GJ} of the respective η' or the η in the Gottfried-Jackson frame of X can also be viewed as understood, since the shapes can be reproduced by the photon acceptance Monte Carlo. As a function of the cosine of the polar angle θ_{GJ} the efficiencies in the photon acceptance and the full Monte Carlo calculation look rather

¹Conseil Européenne pour la Recherche Nucléaire, European Organisation for Nuclear Research

different, which can be due two additional clusters in the full Monte Carlo simulation that may come from secondary charged particles.

Very briefly the Monte Carlo results are compared to real data. Namely the influence of the RICH pipe is compared between the η channel in the photon acceptance Monte Carlo and in real 2008 data. Both show a probability of a single photon to shower in the RICH tube of around 21%. Also the transverse momentum of the η in the lab frame is precisely reproduced in the full Monte Carlo simulation compared to data.

Contents

Abstract	i
1. Introduction	1
2. The COMPASS Experiment	3
2.1. COMPASS Physics	3
2.1.1. The Muon Program	3
Gluon Polarization:	4
Λ and $\bar{\Lambda}$ Polarization:	4
2.1.2. The Hadron Program	4
Primakoff Scattering:	4
Charmed hadrons:	5
Exotic hadrons:	5
2.2. Experimental Set Up	6
3. Theoretical Overview	11
3.1. Mesons and Exotics	11
3.2. The η' and η Decay Channel	13
3.2.1. Diffractive Excitation	16
3.2.2. Two-Body Decay	16
3.2.3. Three-Body Decay	18
3.3. Pair Production	20
4. Monte Carlo Analysis	21
4.1. Software	21
4.2. The Event Generator	22
4.3. Photon Acceptance Monte Carlo Simulation	26
4.3.1. Implementations	26
4.3.2. The Influence Of The RICH Pipe	31
4.4. Real Monte Carlo Simulation	32
4.4.1. Selection Cuts	32
4.5. Comparison Of Acceptances	35
4.6. Comparison With Data	42
5. Conclusion And Outlook	45

A. Appendix	47
A.1. Software Versions	47
A.2. Source Code	47
A.2.1. The Event Generator	47
A.2.2. Photon Acceptance Monte Carlo Simulation	51

1. Introduction

Nowadays the most basic understanding of nature is summarized in the **Standard Model**, describing twelve elementary particles, six leptons and six quarks ,their antiparticles, four principle forces and their respective gauge bosons. One of the four basic forces in nature is the strong force, responsible for the cohesion of the nucleons in atomic nuclei or the interactions between hadrons and quarks. Although there is a lot of ongoing research in the field of hadronic interaction, very little is know about the mysteries of the strong force, which shows a completely different behavior than the other three forces. COMPASS, the **CO**mmon **M**uon **P**roton **A**pperatus for **S**tructure and **S**pectroscopy is one of the many experiments trying to investigate characteristics of strong interaction and properties of hadronic systems. The fixed target experiment, located at CERN¹ in Geneva, Switzerland, is connected to the SPS (Super Proton Synchotron) of the LHC (Large Hadron Collider). The COMPASS collaboration that consists of 26 institutes with more than 240 physicist from all over the world, performs two programs, one with a hadron beam and the other one with a muon beam.

The focus of this bachelor's thesis lies in the hadron program, whose purpose is hadron spectroscopy and the search of exotic mesons produced in diffractive excitation processes. Experimental evidence for exotic mesonic structures, such as glueballs or hybrids, does already exist and main candidates for these new particles are supposed in the final states of the diffractive scattering processes $p\pi^- \rightarrow p\pi^-\eta'$ and $p\pi^- \rightarrow p\pi^-\eta$ [4][23]. To precisely measure the quantum numbers of eventually occuring resonances in these decay channels a partial wave analysis (PWA) is needed. The main concern of this thesis is a Monte Carlo simulation for the $\pi^-\eta'$ and the $\pi^-\eta$ channel to support the PWA with a description of the acceptances of the COMPASS detector responses. The study of these acceptances are important since they directly enter the theoretical framework for the description of resonances through partial waves.

After a quick overview of the COMPASS experiment and its set up in the first chapter of this bachelor's thesis the most principle theoretical concepts of the search for exotics and the Monte Carlo simulation of the diffractive excitation are summarized. Chapter 3 describes the programming of an event generator in some detail before a small photon acceptance (PA) Monte Carlo analysis is performed to gain first expectation for the acceptances and results for future comparison. The PA Monte Carlo program serves for a fast possibility to simulate the acceptances at COMPASS and is used to estimate the influence of the three meter long steal pipe of the RICH detector (**R**ing **I**maging **C**herenkov Counter) in the experimental set up. In the later sections of the same chapter a description of a full Monte Carlo simulation using the software COMGEANT

¹Conseil Européenne pour la **R**echerche **N**ucléaire, European Organisation for Nuclear Research

and CORAL follows and the acceptances of both Monte Carlo procedures, the fast PA Monte Carlo and the full Monte Carlo simulation, are studied and compared with each other. At last a brief comparison of the $\pi^-\eta$ final state in real 2008 data and in the full COMGEANT and CORAL calculation is touched.

2. The COMPASS Experiment



COMPASS, the **CO**mmun **M**uon **P**roton **A**pparatus for **S**tructure and **S**pectroscopy is one of the many experiments at CERN (**C**onseil **E**uropéenne pour la **R**echerche **N**ucléaire, European Organisation for Nuclear Research) located in Geneva, Switzerland. Linked to the Super Proton Synchrotron (SPS) at the Large Hadron Collider (LHC), it is a two stage mass spectrometer for fixed target experiments, providing high luminosity and a good momentum resolution in a wide kinematical regime. After the approval in 1996 by CERN, it was built between 1999 and 2000 to contribute to multiple topics in particle physics such as structure functions of nucleons, spin contributions of their quark constituents, properties of gluons or the search for exotic mesons. To address this abundance of physics fields, COMPASS runs two main programs, the muon program using a muon beam and the hadron program where either pions or kaons are used as beam particles to bombard different targets[6]. After the first test runs in 2002 and the first hadron beams in 2004, 2006 and 2007 were dedicated to the muon program while in 2008 and 2009 COMPASS took data for the hadron program[2]. In the following section the physics of the two programs are briefly described and the basic experimental set up is explained.

2.1. COMPASS Physics

In the following, an overview of the physics of the muon and hadron program at COMPASS is given. With the focus on the hadron program some selected topics are briefly discussed and previous experiments, not only from the COMPASS collaboration, are cited.

2.1.1. The Muon Program

Since experimental results from previous experiments of EMC [1] or SLAC [3] showed that the contribution of the quarks inside a nucleon to its total spin is only around 30%, further investigation of the spin dependent structure function is needed. The muon program at COMPASS has the main goal to find out what carries the spin content of a nucleon and how it is distributed. A polarized muon beam as well as different polarized and unpolarized targets are needed to be able to measure the polarization of either gluons or sea-quarks which are both discussed as the carrier of the residual spin. At COMPASS both competing explanations can be verified.

Gluon Polarization:

With deep inelastic scattering the muon program aims at a direct measurement of the gluon helicity distribution ΔG . In a photon-gluon fusion the polarized muon beam particle interacts with a gluon of the proton target via a virtual photon shown in Figure 2.1.

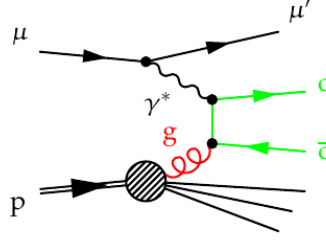


Figure 2.1.: Photon-Gluon Fusion[20]

In the leading order of this process open charm will be produced, which is mainly reconstructed as a neutral D^0 meson and its decay products. This allows the study of a cross section asymmetry for the open charm leptonproduction.

Λ and $\bar{\Lambda}$ Polarization:

Another possible contribution to the nucleon's spin could be carried by strange sea quarks that can be measured via the longitudinal polarization of the Λ and $\bar{\Lambda}$ hyperons, baryons consisting of at least one strange but no charm or bottom quark. With the combination of a polarized muon beam and an unpolarized target one can determine the polarization of a Λ and its strange quark.

2.1.2. The Hadron Program

The hadron program at COMPASS covers three main issues. The polarization measurement of hadronic structures using the Primakoff effect, the investigation of charmed hadrons and the search for exotic states, which is the branch this thesis aims to contribute to. In the next chapter the basic theory about exotic mesons, needed in this thesis is covered.

Primakoff Scattering:

QCD chiral theories give predictions about the polarizabilities of pion and kaons that can be verified at COMPASS using Primakoff scattering.

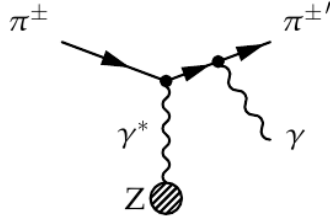


Figure 2.2.: A Primakoff reaction[20]

The Primakoff mechanism (shown in Figure 2.2) can be viewed as the reverse process of the meson decay into two photons. The beam particle Compton scatters off a virtual photon in the Coulomb field of a nucleus with a high charge number in inverse kinematics. Such reactions with a very low momentum transfer between beam and target are important to study mesonic structures.

Charmed hadrons:

Single-charmed and double-charmed baryons are experimentally observed but very little is known about their properties like lifetimes and widths in leptonic and semi-leptonic decays. Investigating these particles is interesting for learning more about the charm quark itself and testing QCD predictions outside the light quark sector.

Exotic hadrons:

Baryons consisting of three quarks qqq , antibaryons made out of three antiquarks $\bar{q}\bar{q}\bar{q}$ and mesons, bound quark anti quark pairs $q\bar{q}$ are the only observed hadrons so far, but many other forms are theoretically predicted. Strongly interacting particles that have not the normal baryonic or mesonic form are called exotics. There are exotic systems consisting of more than three valence quarks for example a pentaquark " $qqqq\bar{q}$ ", flavour blind glueballs, bound states of only gluons " ggg " or a mixture of valence gluons and valence quarks " qqg " called hybrids. Since one can find color neutral combination for all exotics, they are not forbidden by QCD, but they can have quantum numbers J^{PC} not accessible by normal hadrons. Previous experiments already gave evidence for exotic mesons in $\pi^-\eta$ or $\pi^-\eta'$ final states with the forbidden quantum numbers of $J^{PC} = 1^{-+}$. Results of the Brookhaven National Laboratory experiment E852 at the Alternating Gradient Synchrotron (AGS) studying the $\pi^-p \rightarrow \pi^-\eta'p$ final state at an energy of 18GeV/c and a sample of approximately 6000 events, lead to discussions about the existence of an exotic resonance, the $\pi_1(1600)$ [9].

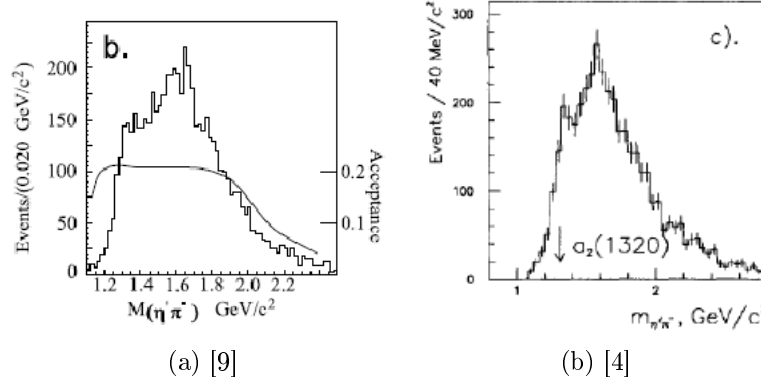
Figure 2.3.: $\pi^-\eta'$ mass distribution

Figure 2.3(a) shows the $\pi^-\eta'$ effective mass distribution recorded in E852. As you can see there is a small peak around 1,3GeV which refers to the known $a_2(1320)$ and a broad enhancement at 1,6GeV. The smooth curve in Figure 2.3(a) shows the acceptance as a function of mass. A partial wave analysis (PWA) of this channel confirmed a resonance at 1600MeV with the exotic quantum numbers $J^{PC} = 1^{-+}$ [9]. The similar VES experiment in 1993 looking at the same $\pi^-\eta'$ effective mass spectrum but in a different decay channel $\pi^-N \rightarrow \pi^-\eta'N$ at 37GeV also saw two peaks for the $a_2(1320)$ and the $\pi_1(1600)$ [4], as you can see in Figure 2.3(b). COMPASS with its ability to use hadronic p , μ , K or π beams and obtain higher statistics, is in a unique position for trying to produce and confirm exotics through diffractive production, explained in the next chapter. In the following section the important parts of the experimental set up of COMPASS for the hadron program is briefly described.

2.2. Experimental Set Up

In this section the most important parts of COMPASS get described and specific experimental properties during the data taking in 2008 are given, because the 2008 data serve as reference for the later described Monte Carlo simulation. For an explanation of the different elements of COMPASS in greater detail I refer to [2]. Figure 2.4 shows the experimental set up with its two stages. In every stage there are detectors for tracking and calorimetry. The first stage detects low energy particles with bigger angles with respect to the beam that defines the z axis, while the second stage covers smaller angles and higher energy of the detected particles.

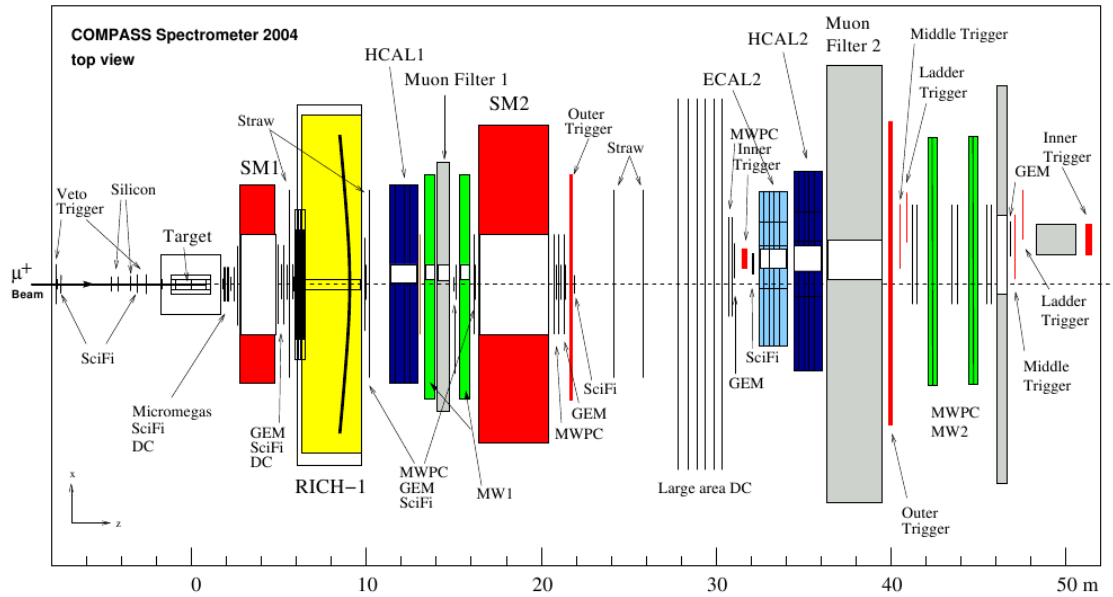
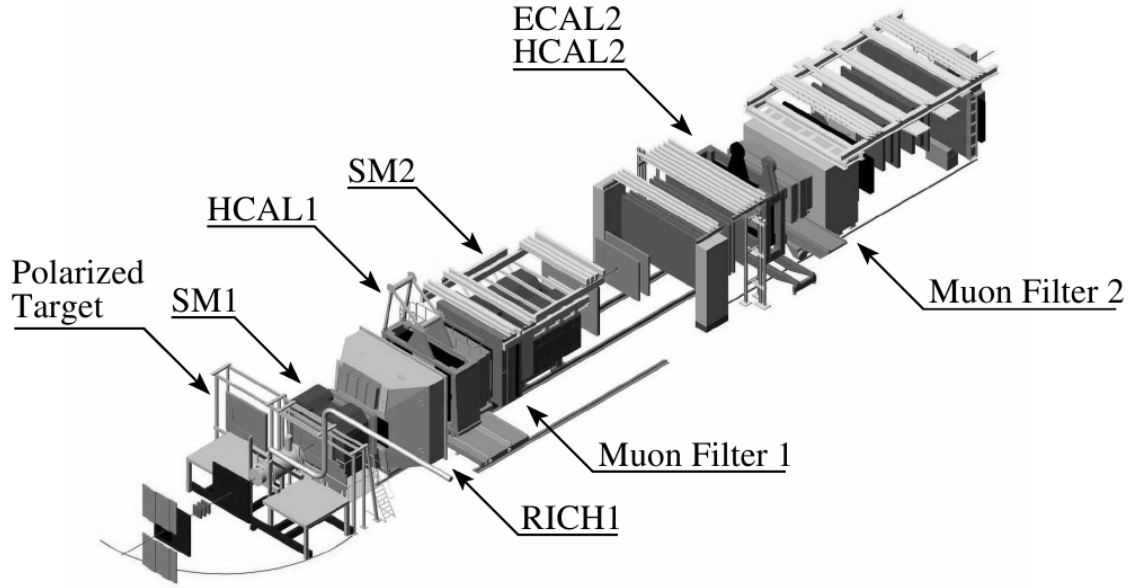


Figure 2.4.: COMPASS set up[2]

The Beam

The COMPASS experiment is connected to the M2 beam line of the SPS (Super Proton Synchrotron) that accelerates protons up to 400 GeV. These protons travel in bunches of 10^{13} particles with a duration of 16,8 ns striking a first target that creates the secondary beam particles for COMPASS, mainly pions and kaons. Momentum filters select the right beam particles needed for a certain experiment. Six percent of the pions and kaons decay into muons and muon neutrinos, $\pi^\pm, K^\pm \rightarrow \mu^\pm \nu_\mu$. While in the muon program

one extracts these muons with the use of hadron absorbers before the beam enters the COMPASS set up, in the hadron program the muons get deflected by other bending magnets to get a pure hadron beam.

The Target

In principle the experimental set up allows to work with a lot of different targets, solid or liquid, polarized or unpolarized. To polarize the target it needs to be cooled with liquid helium down to 200mK and in a process called “dynamic nuclear polarization” it is exposed to a magnetic field of 2,5B and microwaves with a certain frequency. In the muon program one used ${}^6\text{LiD}$ or NH_3 while solid lead and liquid hydrogen targets were installed during the hadron runs. In the data of 2008 underlying this thesis, one used unpolarized liquid hydrogen. Stored in a cylindric cell of 40cm length and a radius of 3,5cm it was also surrounded by the liquid helium cooling.

The Recoil Proton Detector (RPD)

For detecting and reconstruction the recoil proton the **R**ecoil **P**roton **D**etector (RPD) surrounds the target area. It consists of two scintillator rings that measure the time the proton travels between them and its direction. With these measurements one can determine the momentum vector of the recoil proton. The RPD can detect particles in a angular range of 66° to 80° and with momenta greater than 250MeV which means a momentum transfer higher than $t = (p_{\text{target}} - p_{\text{recoil}})^2 = \mathbf{p}_{\text{recoil}}^2 = (250\text{MeV})^2 = 0,06\text{GeV}^2$ [24].

The Ring Imaging Cherenkov Counter (RICH)

The duty of the **R**ing **I**maging **C**herenkov Counter (RICH) is to identify hadrons by their specific Cherenkov ring. It is basically a long iron tube filled with C_4F_{10} gas in which incoming hadrons can travel faster than the speed of light in that gas. Similar to a Mach cone the hadron emits light if it is that fast. In pion-proton diffractive scattering the produced particles have such short lifetimes that they immediately decay within the target region. A lot of them decay into two daughter photons that unfortunately often shower already in the RICH pipe before the electromagnetic calorimeters due to pair production. Thus the RICH detector is not a valuable element in the decay channel studied in this thesis, which gives rise to the question of its absolute influence on the measurements. In chapter 4.3.2 I tried to find ways to investigate the effect of the RICH on the acceptance and compare its simulation with real data.

The Electromagnetic Calorimeters (ECAL1/ECAL2)

The electromagnetic calorimeters ECAL1 and ECAL2 are of major importance in the COMPASS experiment. Since there are mostly decays into charged daughter particles or photons, the reconstruction of the mother particles in the decay chain rely heavily on

the record in the ECALs. Charged particles entering the scintillator emit photons due to bremsstrahlung that convert into electron-positron pairs. These charged electrons and positrons radiate bremsstrahlung again and this chain continues until the energy of the photons is not high enough to build a e^+e^- -pair any more. Of course a photon entering the calorimeter can start the same chain with pair production. All photons produced in the electromagnetic calorimeter together form a so called cluster. The ECALs not only record the positions of these clusters but also their energy.

The Hadronic Calorimeters (HCAL1/HCAL2)

The hadronic calorimeters HCAL1 and HCAL2 are able to detect and measure hadrons that prefer to interact strongly and therefore are less significant in the ECALs. Since all particles in the decay chain studied in this thesis are either charged or photons the hadronic calorimeter are not important, besides one can see a “shadow” of HCAL1 in the record of ECAL2 that is located behind. The HCALs play a more important role in the muon program where they measure for example neutrons from charmed baryon decays or can be used as part of the trigger.

The Trigger

The goal of a trigger system is a preselection of events that are interesting for the physics one wants to study. It rapidly decides by simple criteria, such as the exceeding of detector thresholds while other logical conditions are true, which events to keep and which to already sort out before the total amount of events is recorded. In this thesis with the focus on diffractive production the trigger of choice is the DT0 trigger. It is a combination of other triggers, mainly the beam trigger that selects events where only one beam particle interacted with the target and the RPD trigger that makes clear that there is one recoil proton that can be traced back to the target. The Veto trigger is also part of the DT0. Besides others it marks events where additional particles from hadronic interactions or halo-particles are present in the beam line.

3. Theoretical Overview

This chapter provides the necessary theoretical background knowledge for the physics in this thesis. First a general overview of mesons and exotics is given and special features of the relevant decay channels are shown that are important for the later presented results of the Monte Carlo simulation. Later basic kinematics that is important to program the event generator is presented. To keep this part short, theorems and equations are directly given and not derived. The goal in these sections is to comprise every topic in a few equations or conditions so that they are easy to implement in programming code. The implementation itself is explained in the later chapter.

3.1. Mesons and Exotics

In 1934 Yukawa predicted the existence of a carrier particle of the nuclear force. In his theory nucleons in an atomic nucleus hold together due to the exchange of this carrier particle. He expected the mass of the particle between the mass of leptons (meaning ‘light-weight’) and baryons (‘heavy-weight’) and called it *meson*, from the Greek word mesos, meaning ‘intermediate’[11]. 1947 the first mesons, the charged *pions* π^+ and π^- were discovered with a mass about 273 times bigger than the mass of an electron ($m_{\pi^+, \pi^-} \approx 135\text{MeV}$). Like all mesons, these pions are members of the hadron family, which means that they consist of quarks. Mesons are bound states $q\bar{q}'$ of quarks q and antiquarks \bar{q}' where the flavour of q and \bar{q}' may be different. They are usually characterized by their total angular momentum J , their parity P and their charge conjugation C . J is thereby composed from the total spin S ($S = 1$ meaning parallel and $S = 0$ anti-parallel spin of q and \bar{q}') and the relative orbital spin L of the $q\bar{q}'$ pair, $|L - S| \leq J \leq |L + S|$. P and C are defined as follows[15].

$$P = (-1)^{L+1}; \quad C = (-1)^{L+S}; \quad G = (-1)^I C = (-1)^{L+S+I} \quad (3.1)$$

These properties of mesons allow a classification in J^{PC} multiplets distinguishing among (pseudo-)scalar, (pseudo-)vector and tensor mesons. Table 3.1 gives the lowest lying meson states with their quantum numbers, while Figure 3.1 shows a nonet of some known pseudo-scalar mesons with $J^P = 0^-$.

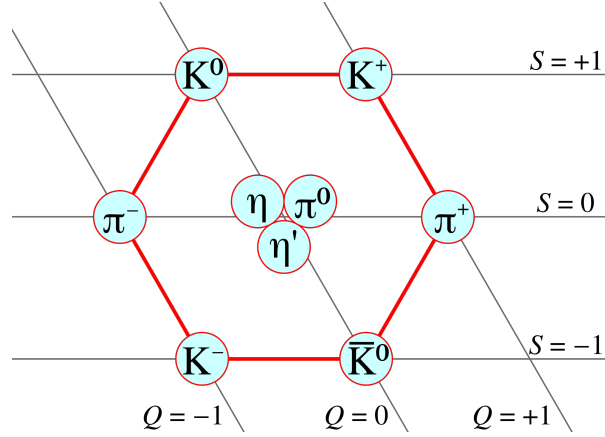


Figure 3.1.: Nonet: pseudo-scalar mesons with $J^P = 0^-$ configuration, different charge Q , spin S , isospin I_3 , [22]

meson type	S	L	P	J	J^P
scalar	1	1	+	0	0^+
vector	1	0	-	1	1^-
tensor	1	1	+	2	2^+
pseudo-scalar	0	0	-	0	0^-
pseudo-vector	0	1	+	1	1^+

Table 3.1.: Different meson types and their quantum numbers

The charge conjugation C is only a good quantum number for neutral mesons that are their own antiparticles like the π^0 or the other mesons in the middle of the multiplet shown in Figure 3.1. Therefore the C -Parity can be generalized to G -Parity defined in Equation (3.1) where I is the isospin. In strong interactions both G and I are conserved. It is apparent from Equation (3.1) that some combination of J^{PC} like $0^{+-}, 1^{-+}, 2^{+-}, 3^{-+}, \dots$ are not accessible in mesonic $q\bar{q}'$ states. An establishment of states with these “forbidden” quantum numbers would be a hint for the existence of non- $q\bar{q}'$ objects with either more than two quarks or gluonic components [21]. Theoretically possible objects occupying forbidden J^{PC} states are glueballs (gg, ggg), tetraquarks ($qq\bar{q}\bar{q}$) and hybrids ($qq\bar{q}$), which are in general referred to as exotics. Some candidates for exotics with $J^{PC} = 1^{-+}$ have been seen in the final states of the $\pi^-\eta'$ - and the $\pi^-\eta$ -system. They are so called *resonances*, intermediate “subatomic particle formations”, visible as peaks in invariant mass spectra. Their very short lifetimes τ give them certain resonance widths $\Gamma = \frac{\hbar}{\tau}$ (\hbar : Planck’s constant). According to the uncertainty principle $\Delta E \Delta t \geq \frac{\hbar}{2}$

a resonance has no well defined mass, but a blurred value Δm .

$$\Delta E \Delta t \geq \frac{\hbar}{2} \quad (3.2)$$

$$\Delta E = (\Delta m)c^2 \quad (3.3)$$

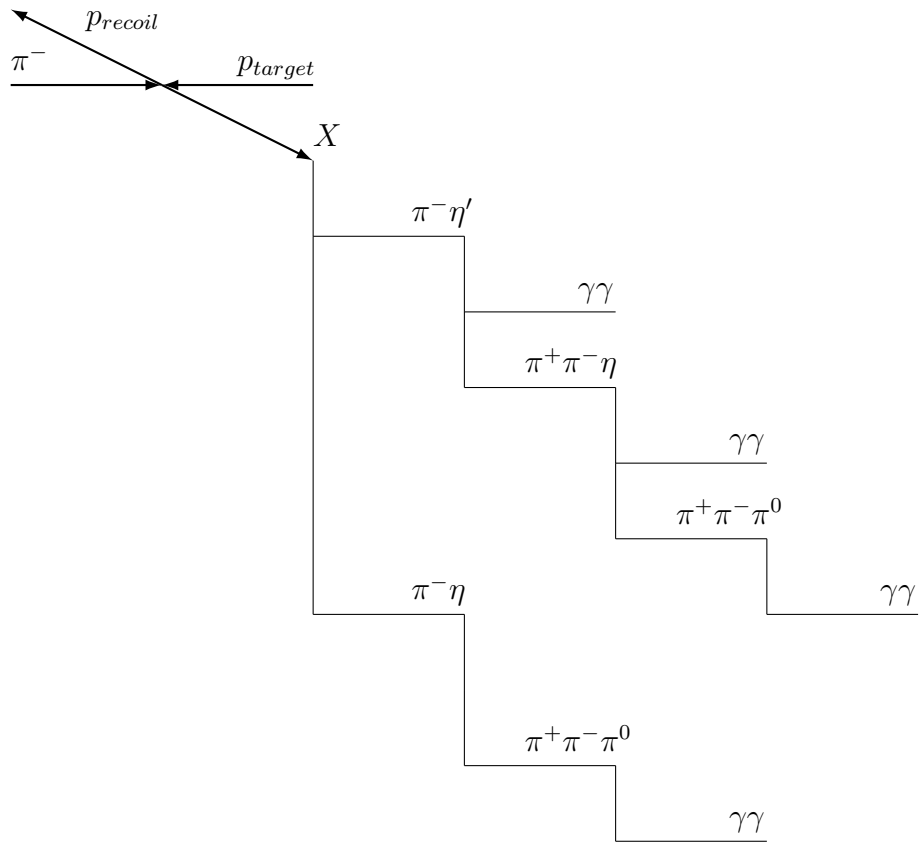
$$\Delta t = \tau \quad (3.4)$$

$$\Rightarrow \Delta m \geq \frac{\hbar}{2\tau c^2} = \frac{\Gamma}{2c^2} \quad (3.5)$$

With extremely short lifetimes even lower than the lifetimes of the decay products ($\tau_\eta = 5,0 \cdot 10^{-19}\text{s}$, $\tau_{\eta'} = 3,2 \cdot 10^{-21}\text{s}$), the mass widths of these resonances would be several MeVs, which makes it experimentally very difficult to observe such broad peaks and assign them to resonances. A good understanding of what is underground and what is physical peaks in a recorded spectrum is needed, which makes a realistic Monte Carlo simulation very important.

3.2. The η' and η Decay Channel

The decay channel of interest with possible candidates for exotics are $\pi^- p \rightarrow \pi^- \eta' p$ and $\pi^- p \rightarrow \pi^- \eta p$ with the η' decaying into two pions and the η s disintegrating to either two photons or three pions. Figure 3.2 schematically summarized every decay that is taken into account for this thesis. In Table 3.2 the final states with their numbers of charged particle tracks and the labeling that is used in the following is shown.

Figure 3.2.: Decay scheme of the η' - and η -channel

$p + \pi^- \rightarrow pX$ $X \rightarrow$	label	number of tracks
$\pi^- \eta'(\pi^+ \pi^- \eta(\gamma\gamma))$	$\eta', \eta \rightarrow \gamma\gamma$	3
$\pi^- \eta'(\pi^+ \pi^- \eta(\pi^+ \pi^- \pi^0(\gamma\gamma)))$	$\eta', \eta \rightarrow \pi^+ \pi^- \pi^0$	5
$\pi^- \eta(\pi^+ \pi^- \pi^0(\gamma\gamma))$	$\eta, \eta \rightarrow \pi^+ \pi^- \pi^0$	3

Table 3.2.: Final states of the decay channels

Data from the COMPASS hadron runs can be selected according to these final states and in the Monte Carlo simulation the whole decay chain is imitated. The first step, where the pion beam hits the fixed proton target $\pi^- + p \rightarrow X + p$, can be simply described as a standard two-body scattering problem. Figure 3.3 visualized this process, $\textcircled{1} + \textcircled{2} \rightarrow \textcircled{3} + \textcircled{4}$. In the following let p_i be the momentum Lorentz vector (4-vector) of a particle $i = 1, 2, 3, 4$ and \mathbf{p}_i the spatial momentum vector (3-vector).

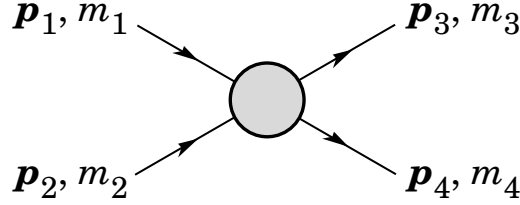


Figure 3.3.: Two-body scattering[15]

The two-body scattering is normally described using the Mandelstam variables s, t, u defined as follows.

$$s = (p_1 + p_2)^2 = (p_3 + p_4)^2 \quad (3.6a)$$

$$t = (p_1 - p_3)^2 = (p_2 - p_4)^2 \quad (3.6b)$$

$$u = (p_1 - p_4)^2 = (p_2 - p_3)^2 \quad (3.6c)$$

$$s + t + u = m_1^2 + m_2^2 + m_3^2 + m_4^2 \quad (3.6d)$$

s is usually referred to as the center of mass energy while t reflects the momentum transmission, which is always negative for scattering processes. In this thesis not only t but also t' is used as a variable for momentum transmission. It is the difference between t and the minimal momentum transmission t_{min} that can be computed with Equation (3.8).

$$t' = |t - t_{min}| \quad (3.7)$$

$$t_{min} = \left(\frac{s + t + u}{2\sqrt{s}}\right)^2 - (p_{1cm} - p_{3cm})^2 \approx \frac{(m_3 - m_1)^2}{4\mathbf{p}_1^2} \quad (3.8)$$

In this simplified picture p_3 would be the Lorentz vector of a resonance X . However the production mechanism of this resonance can not be explained by the two-body

scattering. A more accurate explanation is a *diffractive excitation* of the pion beam particle, a process with a momentum transmission t low enough, so the target proton remains intact, but high enough to excite the pion leading to an appearance of the resonance.

3.2.1. Diffractive Excitation

A detailed look of the pion-proton interaction is shown in Figure 3.4. The process where the pion projectile is scattered off the target proton can be considered to be an exchange of another particle, the *pomeron* \mathbb{P} . It was first predicted by Regge in 1961 in the framework of the so-called *Regge theory*, a set of empirical relations that are not based on Quantum Chromo Dynamics (QCD)[18].

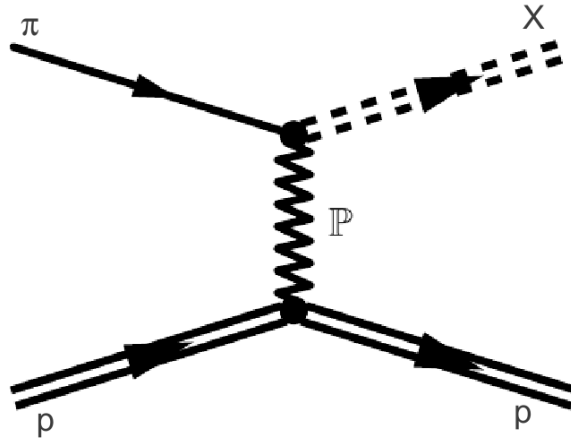


Figure 3.4.: Pomeron exchange in diffractive excitation[10]

The pomeron can be viewed as a multi-gluonic state and is theoretically described by a Reggeon trajectory. The momentum transfer t in a diffractive dissociation process is by definition the squared 4-momentum q of the exchanged pomeron,

$$t = q^2 = (p_\pi^- - p_x)^2 = (E_\pi^- - E_x)^2 - (\mathbf{p}_\pi^- - \mathbf{p}_x)^2. \quad (3.9)$$

The projectile does not directly hit the target proton, but only touches it with an impact parameter that is in the range of the strong interaction ($\approx 10^{-15}$). t is therefore so small that the recoil proton has the chance to remain intact[10].

3.2.2. Two-Body Decay

After the diffractive production of the resonance X , it can disintegrate into a pion and a η' or a η as you can see in Figure 3.2. Figure 3.3 shows a two-body decay scheme in the lab frame.

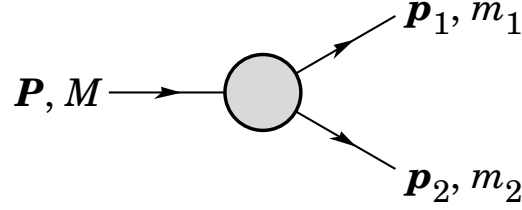


Figure 3.5.: Two-body decay[15]

For convenience this two-body decay is viewed in the center of mass (CM) frame, where the 4-momentum vectors p_1 and p_2 of the daughter particles are parallel, opposite and of same length due to 4-momentum conservation. The energies of ① and ② in the CM-frame are given by Equations (3.10) using natural units with $c = 1$ and assuming s is again the center of mass energy.

$$E_{1cm} = \frac{s + m_1^2 - m_2^2}{2\sqrt{s}} \quad (3.10a)$$

$$E_{2cm} = \frac{s + m_2^2 - m_1^2}{2\sqrt{s}} \quad (3.10b)$$

$$|\mathbf{p}_{1cm}| = \sqrt{E_{1cm}^2 - m_1^2} \quad (3.10c)$$

$$|\mathbf{p}_{2cm}| = |\mathbf{p}_{1cm}| = \sqrt{E_{2cm}^2 - m_2^2} \quad (3.10d)$$

$$(3.10e)$$

To determine these properties not only in the lab frame, but in any other inertial system, one can apply a Lorentz transformation like in Equation (3.11), where E^*/p_{\parallel}^* are the properties in the new system, while E/p_{\parallel} are the ones in the system from which one wants to boost. The \parallel -index of the momenta means that only the momentum components parallel to the boost direction are transformed.

$$\begin{pmatrix} E^* \\ |\mathbf{p}_{\parallel}^*| \end{pmatrix} = \begin{pmatrix} \gamma_f & -\gamma_f\beta_f \\ -\gamma_f\beta_f & \gamma_f \end{pmatrix} \begin{pmatrix} E \\ |\mathbf{p}_{\parallel}| \end{pmatrix} \quad (3.11)$$

The relativistic variables β_f and γ_f of the frame to be changed are computed as follows.

$$\beta_f = \frac{|\mathbf{p}|}{E} \quad (3.12)$$

$$\gamma_f = \frac{1}{\sqrt{1 - \beta_f^2}} \quad (3.13)$$

The relativistic energy momentum relation (Equation (3.14)) is therefor true in every

inertial system.

$$E^2 = \mathbf{p}^2 + m_0^2 \quad (3.14)$$

However with these equations one knows the energies and momenta of every decay product in every inertial system, two variables are still unknown and can not be determined from conservation laws, the orientation of the decay plane described by two spherical angles φ and θ [14].

A very useful inertial system in which the two-body decay of the resonance X is described, is the *Gottfried-Jackson frame*. It is the rotated center of mass system with the beam line as z axis and the xy -plane spanned by the 3-vectors of the recoil proton and the resonance. This system is very important because the angular momentum of the daughter particles can be easily quantized through a projection on the z -axis.

3.2.3. Three-Body Decay

In both decay channels, η' and η in Figure 3.2 you can see the presence of three-body decays, namely $\eta' \rightarrow \pi^+\pi^-\eta$ and $\eta \rightarrow \pi^+\pi^-\pi^0$.

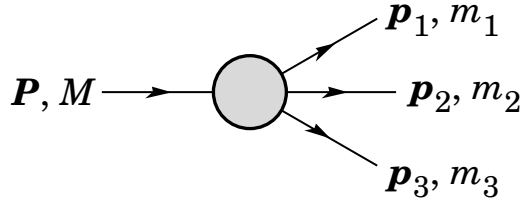


Figure 3.6.: Three-body decay[15]

While in a two-body decay the momenta of the daughter particles are equally distributed with reference to the rest frame of the mother resonance, this is normally not the case in a three-body decay, schematically pictured in Figure 3.6. This manifests itself in an anisotropic phase space with the infinitesimal phase space element

$$dL = \frac{1}{(2\pi)^9} \delta^4(P - p_1 - p_2 - p_3) \frac{d^3\mathbf{p}_1}{2E_1} \frac{d^3\mathbf{p}_2}{2E_2} \frac{d^3\mathbf{p}_3}{2E_3}. \quad (3.15)$$

In 1953 R.H. Dalitz introduced a convenient technique to visualize this phase space, that can be described by only two variables. He took two combinations of the masses of the decay particles, for example $m_{12} = (p_1 + p_2)^2$ and $m_{23} = (p_2 + p_3)^2$ and created a scatter plot with the squares of these variables on the x - and y -axis. This type of scatter plot, now called *Dalitz plot*, provides a very useful tool to study the dynamics of every three-body decay[5].

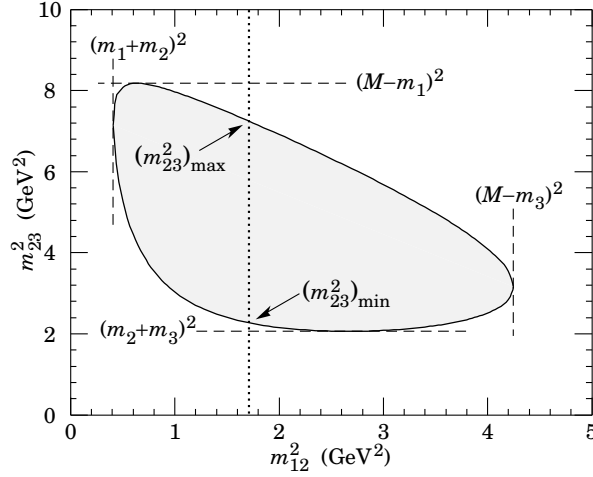


Figure 3.7.: Dalitz plot[15]

Figure 3.7 gives an idea how a Dalitz plot looks like. In the case of an fully isotropic decay, the Dalitz plot would be completely flat, which means that there are no angular correlations between the decay products. Since symmetries or decay mechanisms involving a resonance may impose restrictions on the momentum distribution, the Dalitz plot shows non-uniformities. If the three-body decay is dominated by a resonant process, a peak around the mass of the resonance appears in the Dalitz plot. In the case of the η' - and η -decay, it is acquainted from literature that they neither decay over resonances nor isotropically. For a mathematical description of the form of the Dalitz plot one often uses a certain parameterization called *general decomposition*[19]. Equation (3.18) shows the definition of the variables X and Y for the general decomposition, where T_i is the kinetic energy of the decay product $i = 1, 2, 3$.

$$Q = T_1 + T_2 + T_3 \quad (3.16)$$

$$X = \frac{\sqrt{3}}{Q}(T_2 - T_1) \quad (3.17)$$

$$Y = \frac{m_1 + m_2}{m_2} \frac{T_3}{Q} - 1 \quad (3.18)$$

Because the point density in the Dalitz plot is proportional to the intensities of the three-body final states, the height in the Dalitz plot, or if you wish, the z -axis is a measure of the decay amplitude $|M|^2$. With the general decomposition one can fit the shape of the plot like in Equation (3.19), with A being a normalization factor and a, b, c, d , the fit parameters.

$$|\mathcal{M}|^2 = |A|^2 \{1 + aY + bY^2 + cX + dX^2\} \quad (3.19)$$

This equation allows to reconstruct a weighted Dalitz plot, and therefore a restricted momentum distribution for the decay products, in a Monte Carlo simulation using the

fit parameters obtained from an experiment.

3.3. Pair Production

One possible interaction of electromagnetic radiation with matter is pair production. While pair production refers to the production of a particle-antiparticle pair in general, here only the creation of an electron-positron out of an energetic photon is covered. This process can happen in an interaction of the photon with an atomic nucleus, which takes place if a photon passes through any kind of detector material in the COMPASS set up. In the electromagnetic calorimeters this effect is used to measure the energy of the photon but a photon can hit other elements of the experimental set up before, which means it disintegrates too early for a detection. As you can see later this happens very often, especially in the RICH pipe. The threshold of a e^+e^- pair production is the rest energy of the positron and the electron, $E_{\gamma,min} = 2m_e c^2 = 1,022\text{MeV}$ and the longer the path of a photon going through a material is, the more probable it becomes that pair productions happens. If a photon with an initial intensity I_0 hits a material layer with an thickness x the intensity behind the layer is given by Equation (3.20),

$$I(x) = I_0 \exp(-\mu x), \quad (3.20)$$

where μ is the *mass attenuation coefficient* that depends on the photon absorption cross section σ via Equation (3.21) with N_A as Avogadro's constant and A and ρ the atomic number and the density of the material.

$$\mu = \sigma \frac{N_A}{\rho A} \quad (3.21)$$

For high photon energies this mass attenuation coefficient reaches an asymptotic limit μ_0 of

$$\mu_0 = \frac{7}{9} \frac{N_A}{A} r_e^2 4\alpha Z^2 \ln \frac{183}{Z^{1/3}} = \frac{7}{9} \frac{1}{X_0}. \quad (3.22)$$

The in Equation (3.22) defined quantity X_0 is called the *radiation length*, which is a specific constant for a material. It denotes the thickness of the material, in which the probability for a pair production at high photon energies is given by Equation (3.23)[13].

$$P(\gamma \rightarrow e^+e^-) = 1 - \exp(-7/9) \approx 54\% \quad (3.23)$$

After traveling one radiation length in a material, the probability that a photon did not disintegrate and still exists, decreased by a factor of $1/e$. Equation (3.23) serves as future reference in the next chapter, where the effect of pair production becomes crucial in the implementation of the RICH pipe in the photon acceptance Monte Carlo simulation. For a proper theoretical definition of the radiation length I refer to [5] and [13].

4. Monte Carlo Analysis

Before an explanation of the procedures in the Monte Carlo calculations, a small overview of the used software is given. Afterwards the programming of the event generator is described. Later in this chapter the two Monte Carlo simulations are treated and their results of the acceptances are compared with each other. At the end of this chapter an interesting comparison between the transversal momentum of the η as daughter particle of the resonance X in real data and the full Monte Carlo analysis is started.

4.1. Software

The task for the software chain used in this thesis is to gain useful physics information out of raw, experimental or simulated, data containing only binary detector signals. To achieve this, comprehensive programs and frameworks are required that are already built, tested and available. The software used for this thesis is a mixture of general programs in high energy physics (ROOT, GEANT) and COMPASS specific tools (CORAL, COMGEANT).

The ROOT Framework

ROOT is an object oriented analysis framework widely used in particle physics. Written in C++ it was developed in the 1990's in the context of the NA49 experiment at CERN to handle the impressive amount of data that was produced[17]. High amounts of data can be structured and stored in ROOT files for later visual presentation and evaluation. All plots in this thesis were created in ROOT and the generator for the Monte Carlo simulation is programmed for the CINT C++ interpreter implemented in ROOT.

COMGEANT

GEANT is another tool used in high energy physics programmed at CERN. It is able to simulate detector responses to particle tracks through an experimental set up and represent trajectories in the set up visually[7]. For the COMPASS experiment the specific detector sizes, materials and properties got implemented in the generic GEANT code obtaining the useful tool COMGEANT. Responsible for the simulation of the generated particles in the COMPASS set up with their detector hits it is the back bone of the Monte Carlo analysis.

CORAL

CORAL stands for **C**OMPASS **R**econstruction and **A**na**L**ysis and was developed by the COMPASS collaboration to reconstruct the relevant data like particle trajectories, momenta or charge from the raw detector signal amplitudes and time information obtained from experimental or Monte Carlo output. In the reconstruction the best possible tracks and vertices are interpolated and the cluster position and energy in the calorimeters are determined through shower fits on an event-by-event basis. All these quantities are written into a mDST (**m**ini **D**ata **S**ummary **T**able) , a ROOT file, that can be further deconstructed by PHAST[8].

PHAST

The **P**Hysics **A**nalysis **S**oftware **T**ool PHAST is used to read the mDST output of CORAL. Also written in C++, it allows the user to select information of reconstructed events and filter sub-samples under various conditions. This is done by programming a function called “UserEvent” that PHAST executes for every single event stored in a mDST file. Thus, one can automate different selection routines for different analysis purposes[16].

4.2. The Event Generator

The first part of the Monte Carlo chain is the event generator. Its task is to randomly generate events of the decay of interest. As a C++ code using ROOT libraries it is mainly based on a standard random number generator. Every variable that is also measured in real data needs to be simulated in a way that it reflects a realistic event in the COMPASS experiment. How this is used to end up with a set of Lorentz vectors for every decay particle in the final state is described in the following. In section A.2 in the appendix of this thesis you find source code fragments that were used in the analysis.

Vertex and beam properties:

The first thing that the generator code does is randomly choosing a vertex position. For the z -component a simple random number is uniformly generated in the target area between -70cm and -30cm . The x - and y -component is randomly picked out of a histogram showing a real vertex distribution in 2008 COMPASS data (see Figure 4.1).

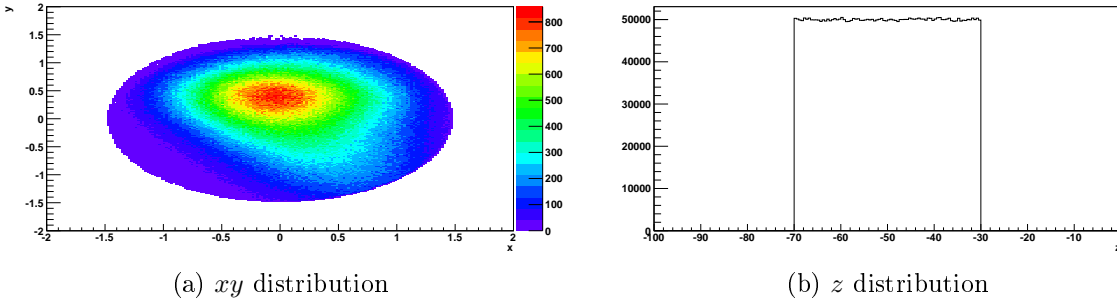
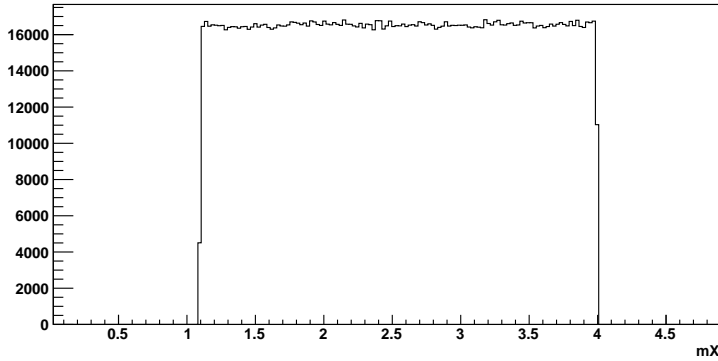


Figure 4.1.: generated Vertex distribution

With a routine programmed by Prometeusz Jasinski the resulting position vector for the primary vertex is used to interpolate a possible direction of the beam. With this direction and a beam energy also created with a random number, but with a Gaussian distribution with $\mu = 191.29(\text{MeV})$ and $\sigma = 1.94476(\text{MeV})$, a Lorentz vector for the beam particle is easily put together, setting its magnitude to $p_{beam} = \sqrt{E_{beam}^2 - m_{\pi^-}^2}$.

Diffraction Production of the resonance X :

In the next step the generator produces a Lorentz vector of a fictitious resonance X . First the mass is uniformly generated in an interval of $[m_{\pi^\pm} + m_{\eta',\eta}, 4\text{GeV}]$, as you can see in Figure 4.2.

Figure 4.2.: Generated mass distribution ($\eta', \eta \rightarrow 2\gamma$)

In the picture of a simple two-body scattering of the beam and the fixed target ($p_{target} = (0, 0, 0, m_p)$), the 4-vectors of the recoil proton and the resonance X are then calculated by generating a Gaussian-distributed random momentum transfer t and using Equations (3.6a). Based on the results of [24] the slope of the generated t' -distribution is 6 so that the simulation matches the situation in real data. In order to simulate a minimal momentum transfer due to the threshold of the RPD (see chapter 2.2) t' starts at 0.1GeV^2 as shown in Figure 4.3.

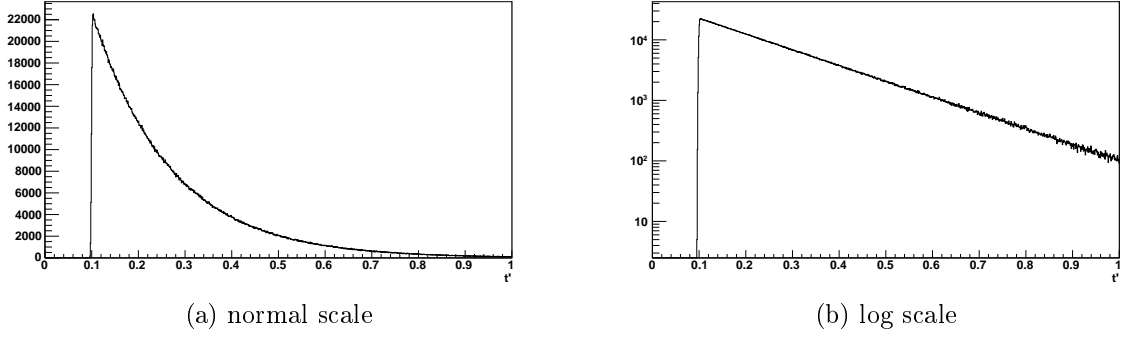


Figure 4.3.: Generated exponential t' distribution with a slope of 6

To get the Lorentz vectors of the resonance X and the recoil proton, one uses Equation (3.6a) to get the angle α between the beam (z -axis) and the resonance X in the CM-frame as follows,

$$t = (p_{beam} - p_X)^2 = p_{beam}^2 + p_X^2 - 2p_{beam}p_X = \quad (4.1)$$

$$= m_{beam}^2 + m_X^2 - 2(E_{beam}E_X - \mathbf{p}_{beam} \cdot \mathbf{p}_X) \quad (4.2)$$

$$\left(\mathbf{p}_{beam} \cdot \mathbf{p}_X = |\mathbf{p}_{beam}| \cdot |\mathbf{p}_X| \cdot \cos \alpha \right) \quad (4.3)$$

$$\alpha = \cos^{-1} \left(\frac{t + 2E_{beam}E_X - m_{beam}^2 - m_X^2}{2|\mathbf{p}_{beam}||\mathbf{p}_X|} \right) \quad (4.4)$$

, where E_{beam} , E_X , $|\mathbf{p}_X|$, $|\mathbf{p}_{beam}|$ are the particle properties in the CM-frame determined with Equations (3.10). Together with a random $\varphi \in [-\pi, \pi]$ reflecting the angle of the decay plane the Lorentz vector of the resonance X and the recoil proton can be set and with a Lorentz boost (Equation (3.11)) transformed in the lab system.

With the simulated resonance X one has to follow the different decay channels from Figure 3.2 and implement all two-body and three-body decays until the final states. This is done by programming a function respectively for every decay and just calling it for the different steps in the decay chain.

Two-body decay:

Boosting in the rest frame of the particle that decays one can simply use Equation (3.10) to compute the energies of the daughter particles. Because the masses of the decay products are known, one can easily determine their momentum $|\mathbf{p}|$ with Equation (3.14). Since there are no restrictions on the direction of the momenta both spatial variables $\varphi \in [-\pi, \pi]$ and $\cos \theta \in [-1, 1]$ are uniformly generated and one obtains enough information to build 4-vectors for every decay product. At the end of the two-body decay function these vectors get boosted in the lab frame.

Gottfried-Jackson frame:

To calculate the kinematically relevant azimuthal and polar angle φ_{GJ} and θ_{GJ} of the η'/η in the Gottfried-Jackson frame of the resonance X , a function is implemented in the code that boosts the Lorentz vector of the η'/η in the rest frame of X and puts up a rotation matrix that immediately rotates it in the GJ-frame with the beam line as the z -axis. Figure 4.4 shows the distribution of the Gottfried-Jackson angles of either the η' or the η which is completely flat.

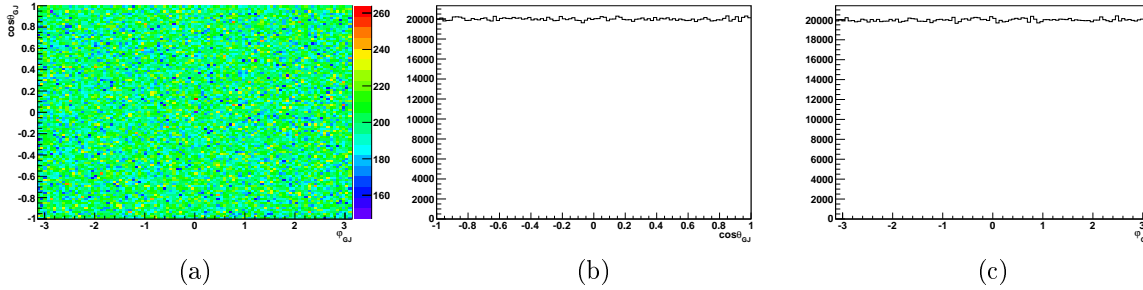


Figure 4.4.: Generated angular distribution of the η'/η in the GJ-frame.

Three-body decay:

In reality the three-body decays of the η' and the η are not isotropic in their phase spaces. This has to be taken into account when simulating these decay processes. Technically the three-body decay is first generated completely flat by introducing another fictitious resonance with random mass $m_{12} \in [m_1 + m_2, M - m_3]$ and applying two two-body decays[14]. To get the weighted distribution the amplitude $|\mathcal{M}|^2$ needs to be calculated according to Equation (3.19) with the fit parameter from Table 4.1. Now these two steps, the uniform three-body decay and the determination of $|\mathcal{M}|^2$, is put in a do-while loop under the condition that $|\mathcal{M}|^2$ is smaller than its maximum value (compare to section A.2 in the appendix). Hence a three-body decay in an event is repeated as long as the intensity of the possible m_{13}^2 - m_{23}^2 -configuration is lower than the maximal $|\mathcal{M}|^2$. In this way one obtains the following anisotropic Dalitz plots in Figure 4.5, that are realistically reproduced in comparison to real data[24].

decay	a	b	c	d	reference
η'	-0, 127	-0, 106	0, 015	-0, 082	[15]
η	-1, 090	0, 124	0	0, 057	[19]

Table 4.1.: Used fit parameters for the Dalitz plots

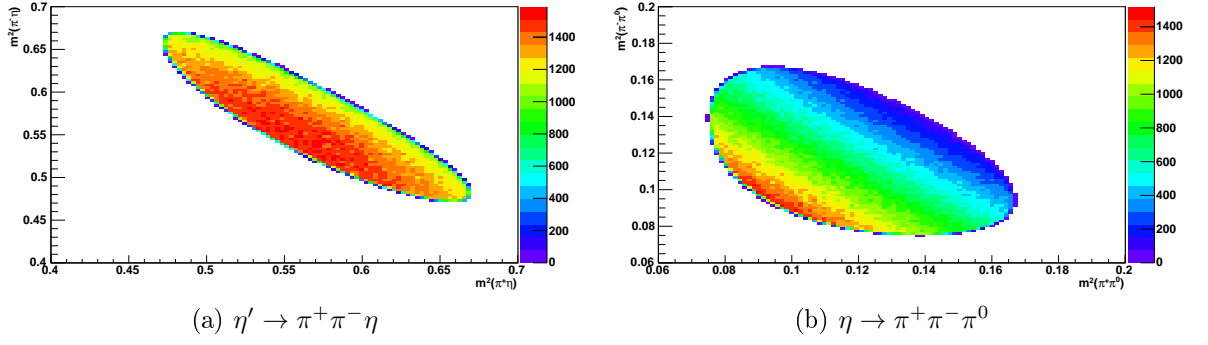


Figure 4.5.: Generated Dalitz plots

Implementing all these steps and ordering the two- and three-body decays by the decay channels one obtains Lorentz vectors for every particle in the respective final states 3.2. These 4-vectors can now be stored in a ROOT tree or printed in a txt-file in order to pass them to the other Monte Carlo programs.

4.3. Photon Acceptance Monte Carlo Simulation

To test the event generator and gain some expectations for the real Monte Carlo results, some elements for simulating the photon acceptance of the experimental set up were added to the generator code. As the name indicates only the photons in the final states of the decays were considered and only a rudimental description of the detectors were implemented. However this approach provides a first heuristic ansatz for an acceptance study and helps to understand the later outcome of a full Monte Carlo analysis. Again the source code can be found in the appendix under section A.2.

4.3.1. Implementations

The only detection elements in the COMPASS experiment implemented in the photon acceptance Monte Carlo selection, sometimes also referred to as “Toy Monte Carlo” or “Fast Monte Carlo”, are the two electromagnetic calorimeters ECAL1 and ECAL2 and the 3,14m long steel tube of the RICH detector that plays a major role in the acceptance of events. In the following the simulation of these detectors are described.

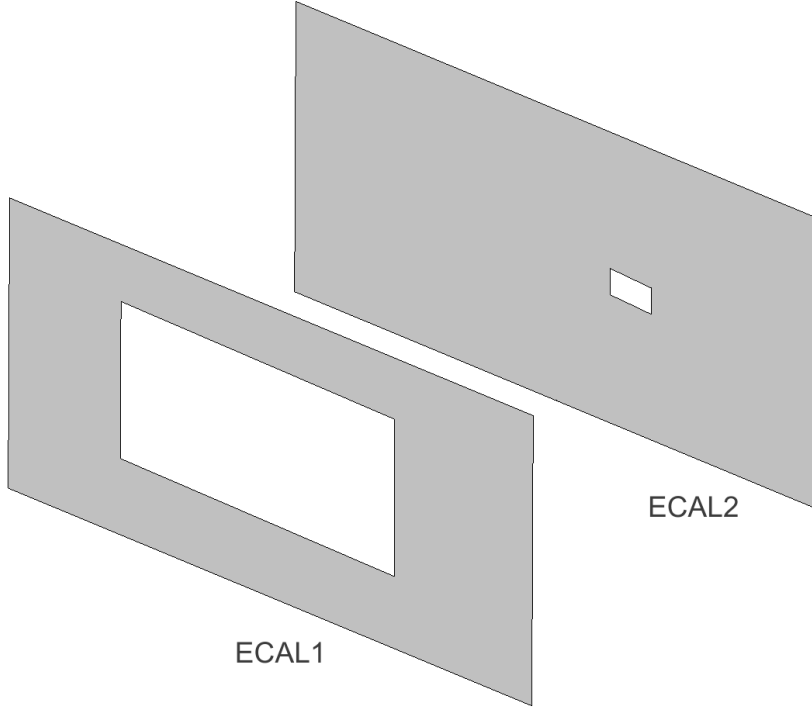


Figure 4.6.: ECALs in the photon acceptance Monte Carlo simulation

ECAL1/ECAL2:

The ECALs are implemented as simple plane areas perpendicular to the beam line and located at the center of the calorimeters, as shown in Figure 4.6. An event is accepted when both photons hit any of the two planes. In Figure 4.6 you can see the ECAL areas with their holes, the exact dimensions can be taken from the source code in section A.2. With the the known 3-momentum of the gammas from the generator one can easily calculate their hit points in the ECAL planes according to Equation (4.5), with \mathbf{r}_{hit} as the position vector of the hit point, \mathbf{r}_{vertex} the generated vertex position, $\nabla\mathbf{p}_\gamma$ the direction of the photon's momentum and λ the distance between the vertex and the hit point.

$$\mathbf{r}_{hit} = \begin{pmatrix} r_x \\ r_y \\ r_z \end{pmatrix} = \lambda \nabla\mathbf{p}_\gamma + \mathbf{r}_{vertex} \quad (4.5)$$

To simulate the threshold of the calorimeters an event is neglected if a photon hits ECAL1 and has an energy smaller than 1GeV or if a photon travels in ECAL2 and its energy is less then 4GeV. Figure 4.7 shows the plot of the photon positions viewed from the beam direction.

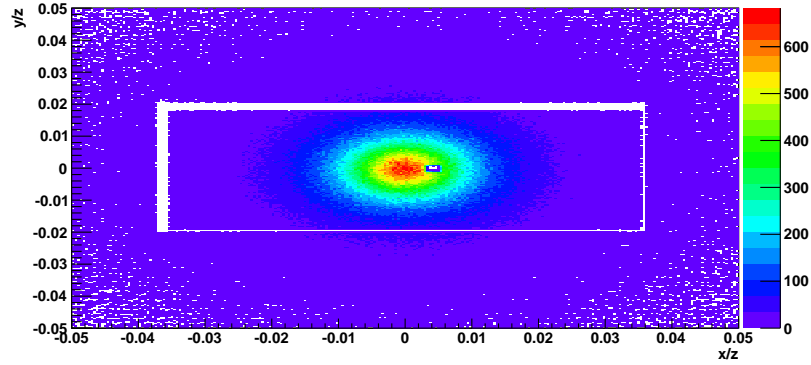


Figure 4.7.: Position of photons in the ECALs

The outer white margin in Figure 4.7 is due to another geometrical cut. Because of the HCAL between the two ECALs in the experimental set up you can also see this 'shadow' in real data, so this is replicated in the code.

RICH:

For some reaction channels it is rather unfortunate that the RICH detector is still a part of the experimental set up in the hadron program. While in the muon program it was of major importance for the identification of kaons from D -meson decays, in the hadron program the RICH pipe is disturbing in the sense that its responsible for a great acceptance loss. To estimate its effect on the photon acceptance a simple geometrical model of the steel tube was inserted in the Toy Monte Carlo program. Figure 4.8 shows the dimensions of the RICH pipe.

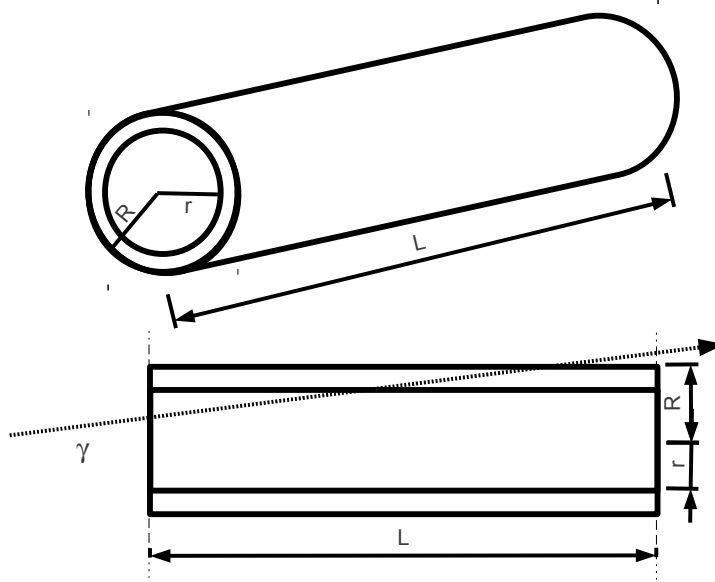


Figure 4.8.: RICH pipe, $L = 314,0\text{cm}$, $r = 4,985\text{cm}$, $R = 5,0\text{cm}$

The code computes the distance a photon traveled in the steel tube in units of radiation lengths. This is computed as follows. First the hit points in the planes at $z_{front} = 591,7\text{cm}$ and $z_{back} = 905,7\text{cm}$, the front and back cover of the steel cylinder have to be determined using Equation (4.5). The distance between these points gives the length of the path the particle travels from the front to the back of the RICH pipe, but it only collects radiation lengths by going through the steel surface of the cylinder. Therefore one needs to find out where the photon enters the pipe surface and where it exits again. This is done by solving Pythagoras' equation twice in the form of Equation (4.6), with $r_{in} = 4,985\text{cm}$ and $r_{out} = 5,0\text{cm}$.

$$(\lambda_{in} p_{\gamma}^{(x)} + r_{vertex}^{(x)})^2 + (\lambda_{in} p_{\gamma}^{(y)} + r_{vertex}^{(y)})^2 = r_{in}^2 \quad (4.6a)$$

$$(\lambda_{out} p_{\gamma}^{(x)} + r_{vertex}^{(x)})^2 + (\lambda_{out} p_{\gamma}^{(y)} + r_{vertex}^{(y)})^2 = r_{out}^2 \quad (4.6b)$$

By solving these quadratic equations, one obtains λ_{in} and λ_{out} giving the distances from the vertex to the position where the photon enters or exits the lateral surface of the RICH pipe. Thereby the positions of the photon entering and leaving the steel surface are determined and the path of a photon through the steel can be calculated and divided by the specific radiation length of iron which is $X_0(Fe) = 1,76\text{cm}$. Figure 4.9 shows how many radiations lengths are collected by a single photon.

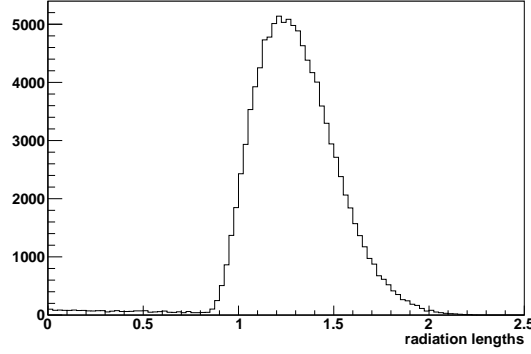


Figure 4.9.: X/X_0 of a photon hitting the RICH pipe

To simulate the pair production in the RICH pipe that would make a real event useless for experimental investigations the program cuts out events if the calculated number of radiation lengths is greater than a random number exponentially distributed with a slope of 7/9, based on Equation (3.23). This means that one loses many events where photons hit the tube of the RICH detector, which leads to a circular shadow structure in the middle of ECAL2 that is clearly visible in Figure 4.7, which shows the same plot as Figure 4.10 but with the implementation of the RICH pipe.

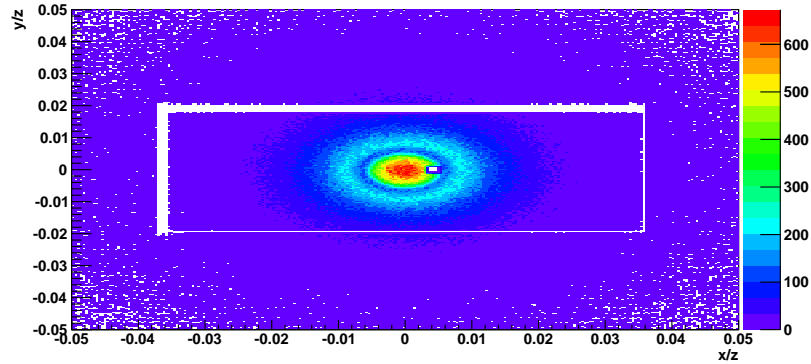


Figure 4.10.: Position of photons in the ECALs with an implemented RICH

Since this loss of events where photons already shower in the RICH pipe before they can be detected by the electromagnetic calorimeters is an inconvenient effect in the experiments, one would like to know the absolute value of the decreased acceptance and

whether it can be simulated realistically in the fast Monte Carlo. Therefore in the next section 4.3.2 2008 data from week 37 selected for the η -channel with the η decaying in $\pi^+\pi^-\pi^0$ is compared with the RICH simulation.

4.3.2. The Influence Of The RICH Pipe

For a reasonable comparison between the observed data and the RICH simulation in the photon acceptance Monte Carlo one would like to investigate the influence of the RICH pipe on a single photon. A comparison of plots like in Figure 4.10 and Figure 4.10 is not so clear since an event is already cut out even if only one of the two photons in the final state hits the RICH pipe not taking the other photon into account. To overcome this problem one only looks at one photon in the event with the condition that the other photon flew unaffected through the RICH pipe. In the program this is down by a query whether the distance of a photon from the z axis in the ECAL2 is smaller than the radius of the RICH pipe, if yes, the other photon in the final state of the event is plotted. In the case where both photons do not touch the RICH pipe one photon is chosen randomly. The histograms in Figure 4.11 show the radii of the photon hit points in ECAL2 plotted in this way.

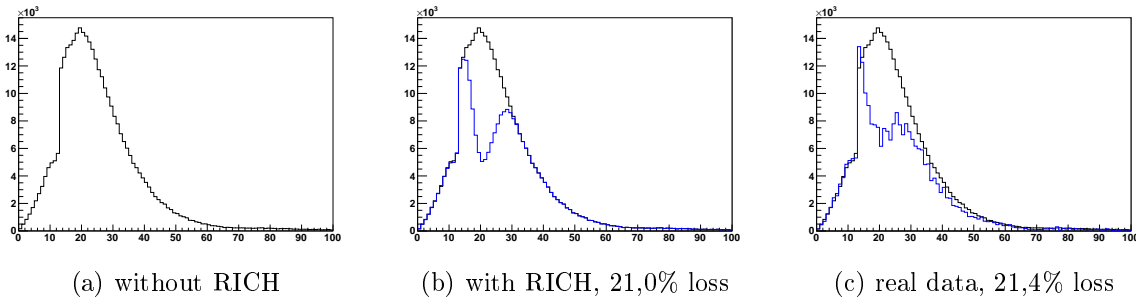


Figure 4.11.: Radii of photons in ECAL2

The left picture shows the radii of the photon in the photon acceptance Monte Carlo without a cut on the radiation lengths so the effect of the RICH pipe is switched off. The picture in the middle shows the same curve in comparison to the radii of the photons with the presence of the RICH pipe (blue line). The local minimum reflects the shadow of the RICH pipe in Figure 4.10. A comparison of the integrals of the two curves gives the total loss of around 21,0% because of the RICH pipe alone. For a comparison of this loss in the fast Monte Carlo with the percentage loss in real data, the same curve without the RICH (black line in the right picture) is scaled down to the real data plot of the photons' radii (blue line in the right picture). The scaling factor is tuned according to the match of the right and the left tails of both curves. The difference of the resulting curves is 21,4% which gives evidence that the effect of the RICH on the photon acceptance is rather well understood and its simulation is quite realistic in the observed η -channel. The agreement of the middle and the right panel in Figure 4.11 is

not perfect. This is possibly due to misalignment of the RICH tube or to a different influence of the selection criterion that exactly two photon clusters are observed (see next section).

4.4. Real Monte Carlo Simulation

With the event generator for the diffractive excitation in the η' - and η -channel one can start the real Monte Carlo Simulation for the COMPASS experiment. All generated Lorentz vectors of the particles in the final state together with the vertex position are written in a text file to pass it into the COMGEANT program. COMGEANT simulates the behavior of these particles in the different materials of the experimental set up and notes every detector hit. All generated information is stored in mDst.root files that are similar to real data. In a next step CORAL runs over these files and tries to reconstruct a track for different detector signals corresponding to recorded particles. The CORAL output is again saved in ROOT-files from where the PHAST software is used to visualize different properties of the whole simulation and pull out comparable results. This is done for the two final states of the $\pi^-\eta'$ -system and the $\pi^-\eta$ -channel with $\eta \rightarrow \pi^+\pi^-\pi^0$ and the Monte Carlo results are compared with the simple photon acceptance simulation.

4.4.1. Selection Cuts

The UserEvent function called event-by-event in the PHAST program is responsible for the selection of the reconstructed event in the CORAL output. CORAL cannot reconstruct all events that are generated and sometimes it associates more tracks to an event than there is particles in the generated events. For this reason one needs to cut on properties specific for the respective decay channel. The individual cuts are explained in the same order as implemented in the UserEvent function.

- **DT0-Trigger:** The first cut makes sure that the event did not set off the DT0-Trigger.
- **One beam particle:** Events where more than one beam particle flew in the target region are discarded as well.
- **One best primary vertex:** CORAL may rebuild several vertices per event, but only primary vertices, which can be connected to the beam track, are of interest. It happens that there are more than one primary vertex, in this case PHAST selects only the best primary vertex, which is the one with the most tracks.
- **Number of tracks:** To make sure that the number of charged particles in the final states are the same in the input and output of the reconstruction one needs to cut on the number of tracks sprung from the best primary vertex. Therefore events with three tracks from the best primary vertex are selected for the $\eta', \eta \rightarrow \gamma\gamma$ and $\eta, \eta \rightarrow \pi^-\pi^-\pi^0$ channel and five tracks for $\eta', \eta \rightarrow \pi^-\pi^-\pi^0$ (see Table 3.2). Although this cut on the tracks coming out of the best primary vertex reduces

the number of bad events drastically, there are still a lot of events with more than three or five charged particle tracks as you will see later in this section.

- **Charge Conservation:** Reconstructed events that miss charge conservation are also thrown away.
- **One track in the RPD:** Only events are selected, where there is one reconstructed track in the RPD.
- **Two good clusters:** Comparable to the cut on the right number of tracks of charged particles, the cut on two clusters in the ECALs ensures that there are only two neutral photons that shower in the ECALs. A good cluster is one, where there is no reconstructed particle track pointing to it. Still this is not enough and the clusters also have to fulfill other condition, namely their energy must be greater than 1GeV if the cluster is located in ECAL1 and greater than 4GeV in ECAL2.
- **Exclusivity:** In the UserEvent function there is also a query whether the event is exclusive meaning energy is conserved. If the total energy of all final particles is not in a range between 180GeV and 200GeV the event is also thrown away.
- **Reconstructed invariant $\gamma\gamma$ mass:** Last the reconstructed invariant mass of the two photons is only allowed in a certain interval around their parent particle's mass. In the case of the photons originating from a η , $m(\gamma\gamma) \in [0, 43\text{GeV}; 0, 63\text{GeV}]$ and in the case of a π^0 being the parent particle $m(\gamma\gamma) \in [0, 110\text{GeV}; 0, 170\text{GeV}]$.

This wealth of selective cuts lets the initial amount of events shrink dramatically to a small subsample of events that fulfill the above conditions. The cutflow diagrams in Figure 4.12 show how many events are still in the sample after each cuts. As you can see the biggest drop of events is due to the cut on the number of tracks leaving the best primary vertex. Since it is more unlikely to correctly reconstruct five particle tracks than only three, the loss is even more dramatic in the case of the $\eta', \eta \rightarrow \pi^+\pi^-\pi^0$ simulation. The second hardest cut is the one on two good clusters, where in the case of $\eta \rightarrow \gamma\gamma$ the number of accepted events drop by an approximated factor of 2, while in the other two cases with $\eta \rightarrow \pi^+\pi^-\pi^0$ the number of events decrease by a factor of around 3 to 4.

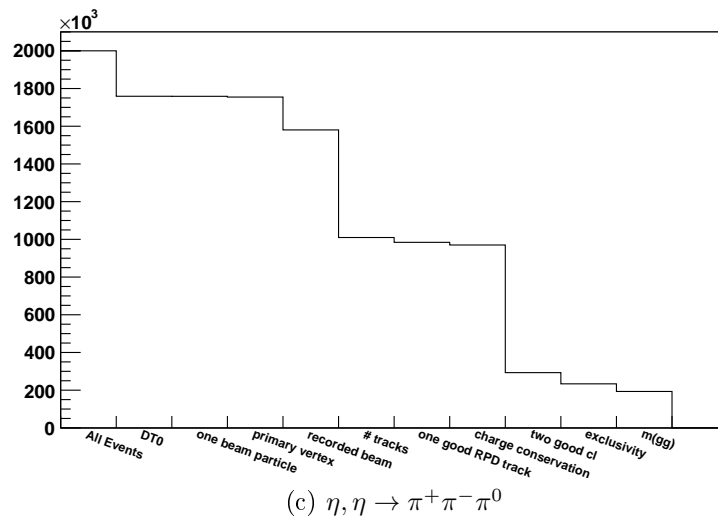
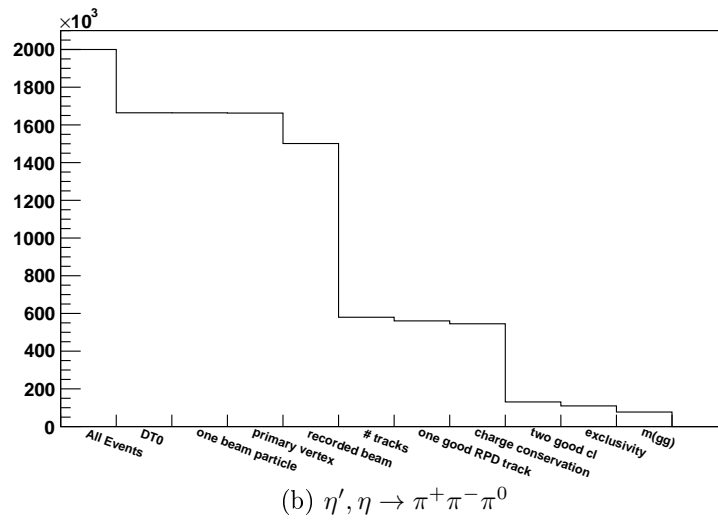
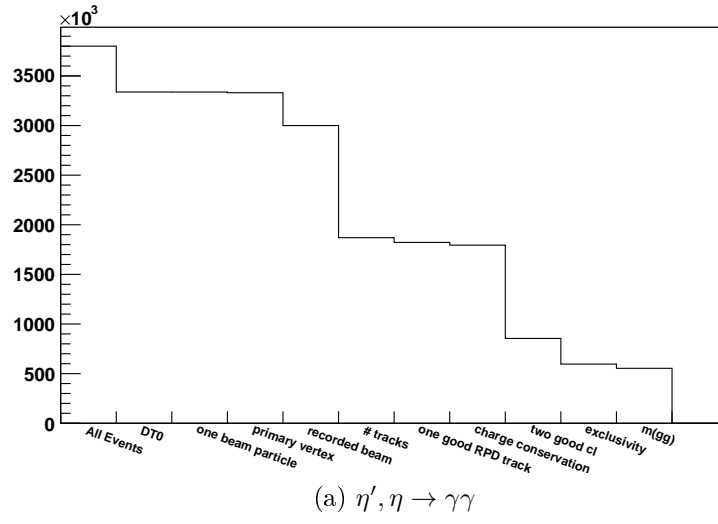


Figure 4.12.: Cutflow diagrams

4.5. Comparison Of Acceptances

After the selection of good events in the Monte Carlo outcome one can start to study the acceptance as a function of various variables. Technically this is done by plotting a certain reconstructed distribution in a histogram and dividing it by the respective *Monte Carlo truth*, the generated distribution put in the Monte Carlo chain. Figure 4.13(a) shows the generated z -distribution of the vertex position in the η' -channel, with $\eta \rightarrow \gamma\gamma$, while in Figure 4.13(b) you can see the vertex position in z after the selection cuts. Obviously the position distribution of the vertex in the z -direction is not flat like it was generated by the event generator. Hence the acceptance shown in Figure 4.13(c) is not uniform.

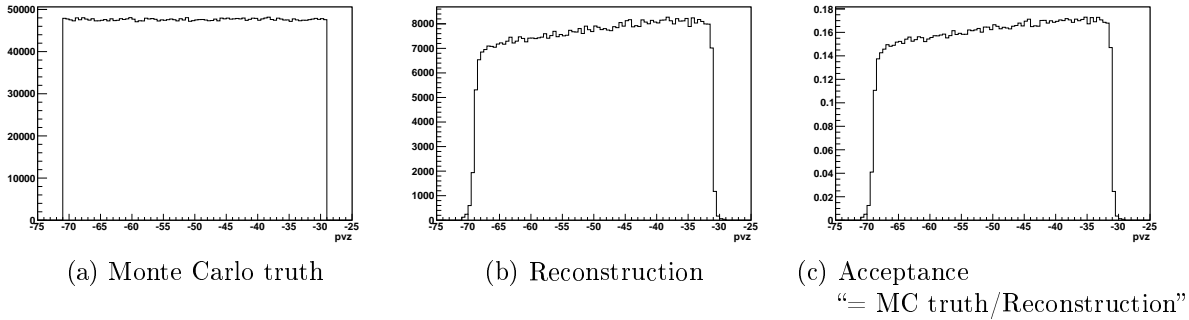


Figure 4.13.: z -distribution of the vertex position in the $\eta', \eta \rightarrow 2\gamma$ event class.

In the following the acceptances for the different final states as a function of different variables are compared between the photon acceptance Monte Carlo and the full Monte Carlo.

z -distribution of primary vertex:

Figure 4.14 shows the acceptance as a function of the z direction of the vertices for all considered decay channels in the full Monte Carlo (red lines) in comparison to the fast Monte Carlo simulation (black lines). In the Fast Monte Carlo you can see a small negative slope of the acceptance over the z -position of the vertices. This could be explained by the fact that the further back the vertex lies in the target the bigger is the gap between ECAL1 and ECAL2 in which a photon may fly that is consequently not seen. In the real Monte Carlo however there is a clearly opposite effect where the acceptance is lower if the vertex is closer to the beam. In this case it is simply the more detector material that the photons have to pass on the way to the calorimeters, in which they gain radiation lengths and are more likely to shower before a detection. The effect is not clearly visible in the $\eta', \eta \rightarrow \pi^+\pi^-\pi^0$ selection where there are the most charged tracks to be reconstructed and the acceptance may rely more strongly on the detection of the pions in the decay's final state. Since there is no charged particle detection implemented in the photon acceptance Monte Carlo calculations, the acceptances are always higher

than in the full Monte Carlo simulations, which becomes clear when looking at the two different scales on the left and the right edge of every subfigure.

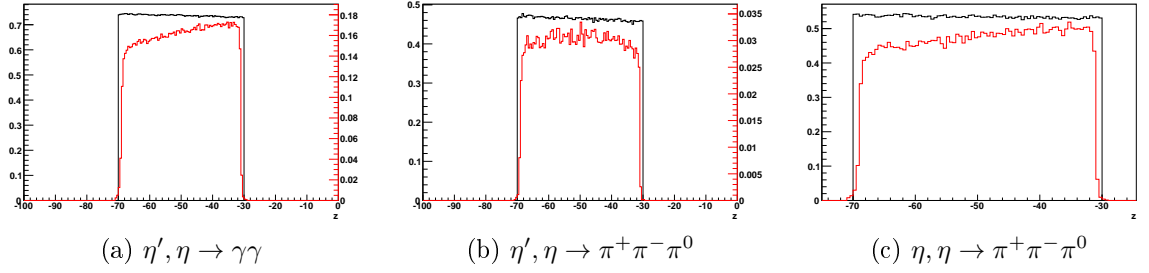


Figure 4.14.: acceptance in z -distribution of the vertex position,
red lines: Full Monte Carlo
black lines: Fast Monte Carlo

xy -distribution of primary vertex, t' , Dalitz plots:

In the same way as the acceptance in the vertex z -distribution, other variables are studied. As it turns out the acceptance as a function of xy -distribution of the vertex position is completely flat in every considered decay chain as well as the t' -distributions, and the Dalitz plots. In Figure 4.15 the acceptance plots for these variables in the $(\eta', \eta \rightarrow \pi^+\pi^-\pi^0)$ - and the $(\eta, \eta \rightarrow \pi^+\pi^-\pi^0)$ - channel are presented representative for the simulations of the other decay channels.

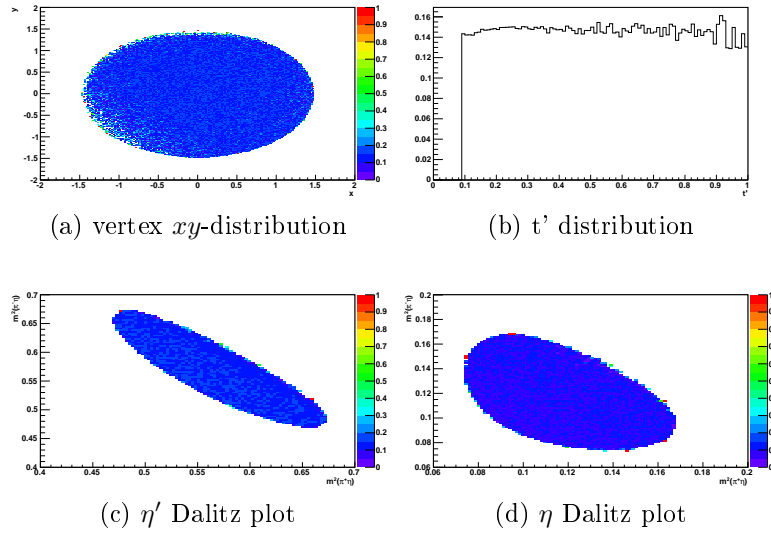


Figure 4.15.: Uniform acceptances in all simulated decay channels

These results of the real Monte Carlo analysis can be perfectly reproduced with the

photon acceptance Monte Carlo where the acceptances for the same variables are also uniform, as you can see in Figure 4.16.

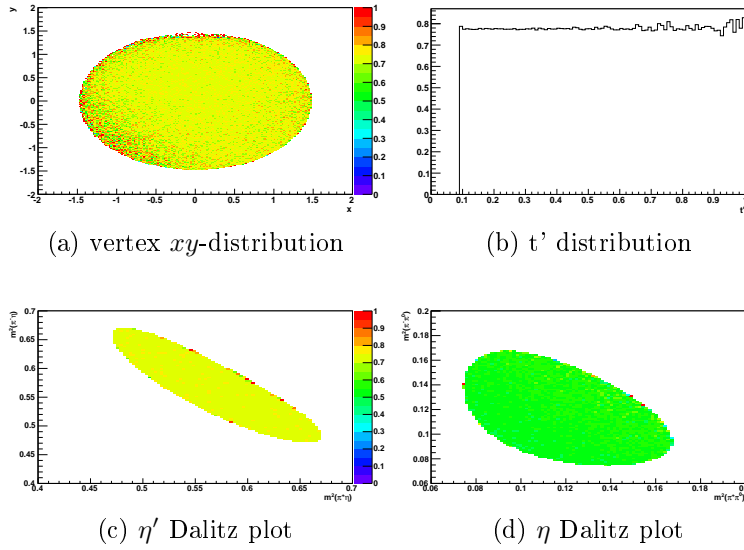


Figure 4.16.: Uniform acceptances in the photon acceptance Monte Carlo

Mass of resonance X :

Another acceptance effect that is not totally flat but can be roughly reproduced by the fast Monte Carlo is found in the mass distribution of the generated resonance. In Figure 4.17 you can see the acceptance as a function of m_X in the real Monte Carlo (red lines) and in the fast Monte Carlo (black lines). The black scales on the right of every subfigure refer to the full Monte Carlo and the red scales on the left refer to the fast Monte Carlo calculations. Although the effect is small, one can see an increase in the mass acceptance towards large m_X .

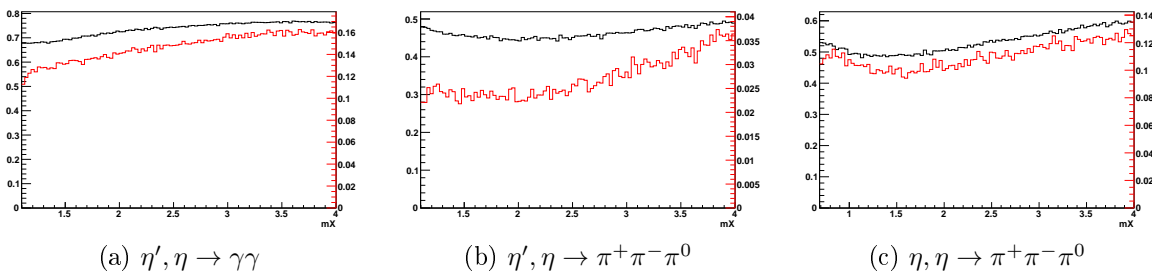


Figure 4.17.: Acceptance as function of $m(\pi^-\eta')$ or $m(\pi^-\eta)$,
red lines: Full Monte Carlo
black lines: Fast Monte Carlo

Since this effect arises in the fast Monte Carlo as well as in the real Monte Carlo equally, it has to be of purely geometrical nature. Its explanation has to do with the greater decay angle of high energy particles. A high initially generated resonance mass means higher energies for all particles in the decay chain due to simple 4-momentum conservation. The last decay in every considered decay chain is a η or a π^0 disintegrating into two photons. If these parent particles have lower energies the photons will have smaller spatial angles, so less transversal momentum and they may fly in the hole in the central region of ECAL2, which lets the acceptance decrease. Higher energies of the parent particles lead to higher spatial angles and the photons are more likely to be detected.

Gottfried-Jackson angles of η'/η :

For a further partial wave analysis of the $\pi^-\eta'$ - or the $\pi^-\eta$ -systems the important variables are the spatial angles φ_{GJ} and θ_{GJ} of the η'/η in the Gottfried-Jackson frame of the generated resonance X . Figure 4.19 and 4.18 show the acceptances for these angles.

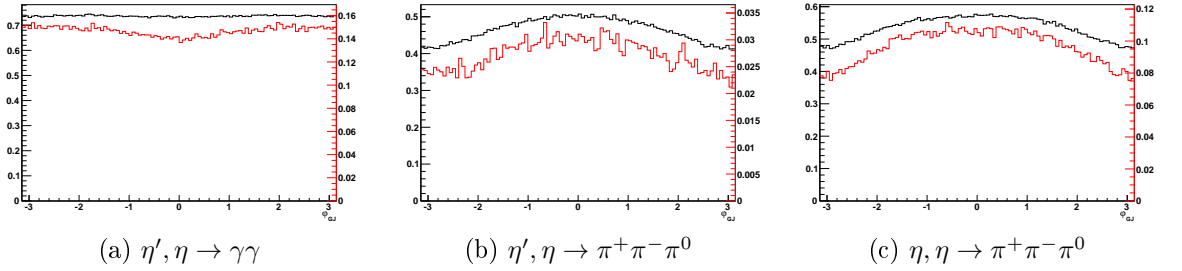


Figure 4.18.: Acceptance as function of φ_{GJ} of η'/η

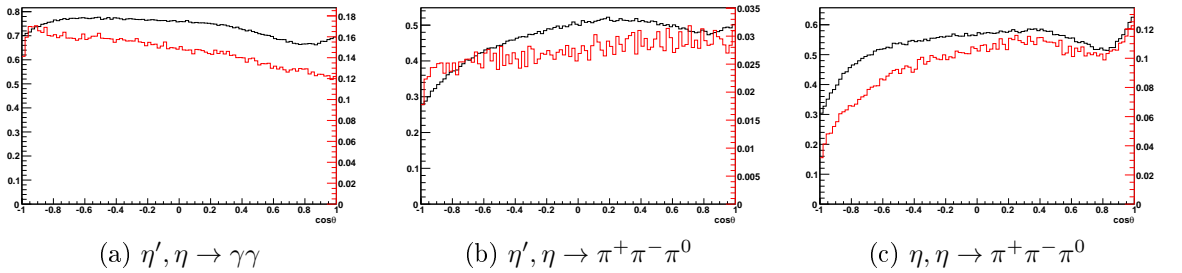


Figure 4.19.: Acceptance as function of $\cos\theta_{GJ}$ of η'/η

As a function of the azimuthal angle φ_{GJ} the acceptances look flat with a shallow minimum in the $\eta \rightarrow \gamma\gamma$ case and a shallow maximum in the $\eta \rightarrow \pi^+\pi^-\pi^0$ cases, where the shape of the curves can be reproduced really well by the photon acceptance Monte Carlo simulation. As a function of the polar Gottfried-Jackson angle θ_{GJ} the

acceptance shows a deep minimum in the $(\eta, \eta \rightarrow \pi^+\pi^-\pi^0)$ -channel at $\cos\theta_{GJ} = -1$, where the η s are emitted backwards. The dependence of the acceptance on the polar angle θ_{GJ} in the other channels do not agree with the photon acceptance Monte Carlo, which indicates a strong influence of the charged particle detection efficiencies in the real Monte Carlo simulation. Remarkable are the local minima around $\cos\theta_{GJ} = 0, 8$ in the fast Monte Carlo histograms, that are also present in the real Monte Carlo acceptance for the $\eta, \eta \rightarrow \pi^+\pi^-\pi^0$ case.

Mass of resonance X vs. $\cos\theta_{GJ}$:

To study the correlation between the generated mass of the resonant system and the direction of the momentum of the decay product η' or η , one plots m_X versus the cosine of θ_{GJ} as done in Figure 4.20. To depress statistical fluctuations and for better comparison the plots for the real Monte Carlo acceptances are rebinned.

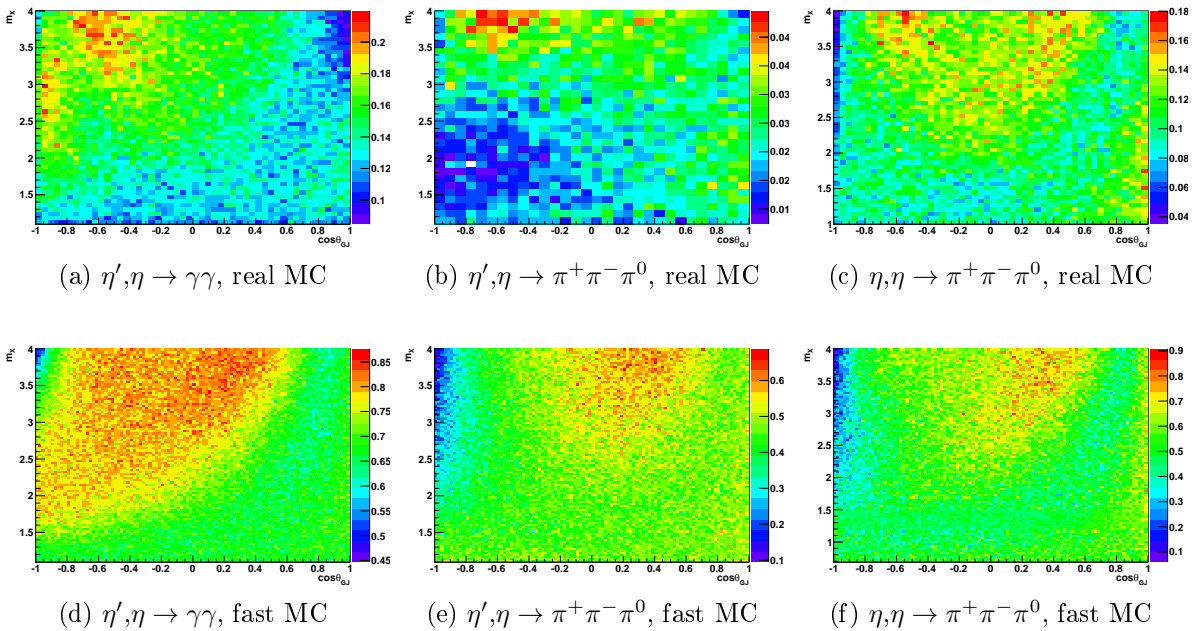


Figure 4.20.: Acceptance in m_X vs. $\cos\theta_{GJ}$

Again the fast Monte Carlo resembles the real Monte Carlo better in the $(\eta', \eta \rightarrow \gamma\gamma)$ - and especially in the $(\eta, \eta \rightarrow \pi^+\pi^-\pi^0)$ -channel while in the $(\eta', \eta \rightarrow \pi^+\pi^-\pi^0)$ -case the two differ a lot. Noticeable is the acceptance drop for high masses and $\cos\theta_{GJ} = -1$ that is apparent in all channels as well as the band of decreased acceptance from high masses and $\cos\theta_{GJ} = 1$ to low masses and $\cos\theta_{GJ} = -1$. The second is due to the RICH pipe as a comparison to the fast Monte Carlo without the cut on the radiation lengths shows. Figure 4.21 shows the same acceptance plot in the photon acceptance Monte Carlo where the RICH pipe is switched off so only the acceptance effects of the

threshold and geometry of the ECALs are taken into account. The band of acceptance loss in the fast Monte Carlo pictures in Figure 4.20 disappears.

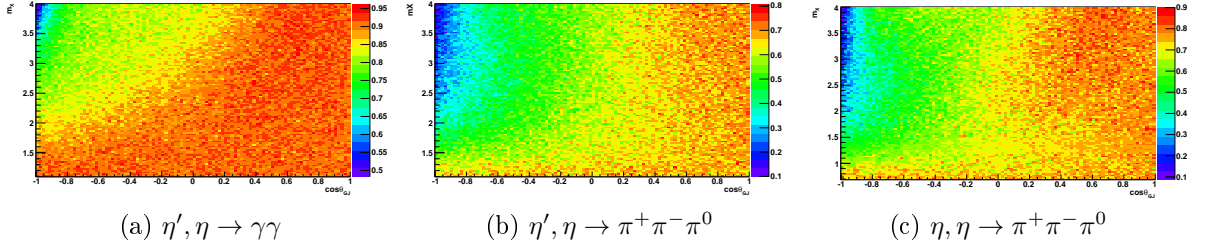


Figure 4.21.: Acceptance in m_X vs. $\cos\theta_{GJ}$, fast MC without RICH pipe

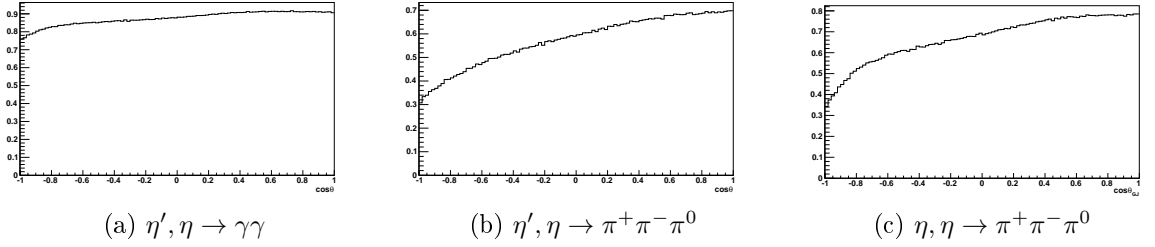


Figure 4.22.: Acceptance in $\cos\theta_{GJ}$, fast MC without RICH pipe

If one looks at the $\cos\theta_{GJ}$ acceptance in the photon acceptance Monte Carlo without the RICH (Figure 4.22) the local minimum at a forward emission with $\cos\theta_{GJ} = 0,8$ disappears, too. This may mean that the RICH description in the full Monte Carlo with COMGEANT and CORAL does not reproduce the effect of the RICH in the η' -channels very well. Remarkable is the amount of clusters in ECAL1 and ECAL2 that are due two secondary charged particles. As you can see in Figure 4.23 that shows the number of reconstructed clusters. There are in average between 18 to 20 clusters in every observed decay channel. These secondary clusters are not all “good” clusters (see section 4.4.1) so most of them are below the ECAL energy thresholds or can be associated to a charged particle track, but still there are often more than two good clusters in the ECALs as Figure 4.24 shows. As compared to the photon acceptance Monte Carlo simulation, the relative yield of one-good-cluster events is also increased in the full Monte Carlo simulation. These clusters could let the efficiencies in the photon acceptance Monte Carlo and the real Monte Carlo differ significantly, since this effect is not taken into account in the photon acceptance Monte Carlo analysis. This might be the reason for the differences of the fast and the full Monte Carlo calculations for the acceptance as a function of $\cos\theta_{GJ}$ in the η' decay channels.

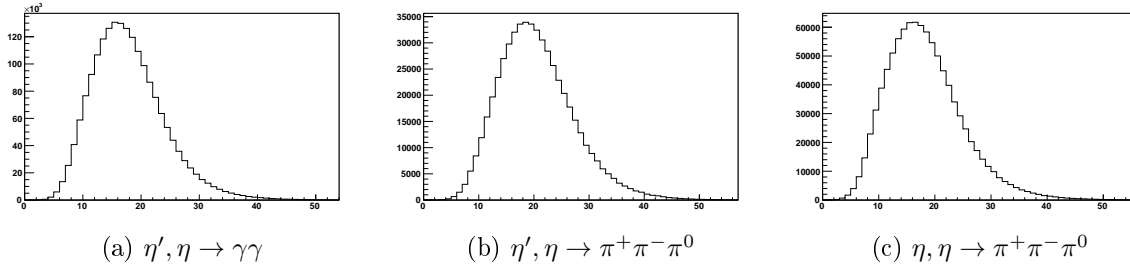


Figure 4.23.: Number of reconstructed clusters in the ECALs

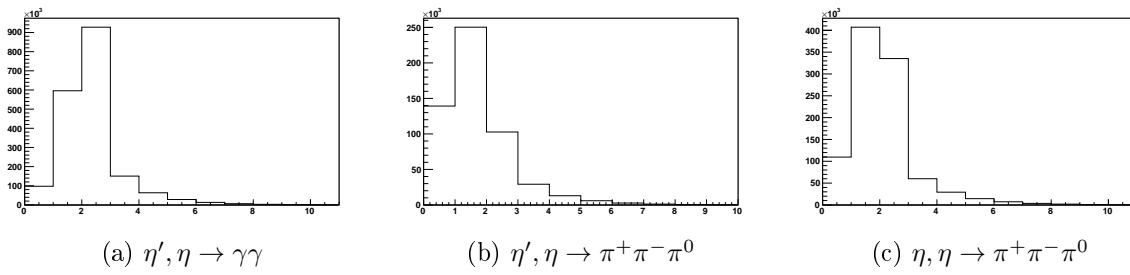


Figure 4.24.: Number of good clusters in the ECALs

The same histograms for the photon acceptance Monte Carlo simulation are shown in Figure 4.25. The whole reaction mechanism of photons creating clusters is not implemented, so you only see the number of detected photons per event. It is not visible that the first bin in all three histograms in Figure 4.25 is not completely empty, but there are only 300 to 400 events where both photons do not fly in the electromagnetic calorimeters. Since there are only two generated photons in an Monte Carlo event, it is impossible to end up with more than two unlike in the real Monte Carlo calculation.

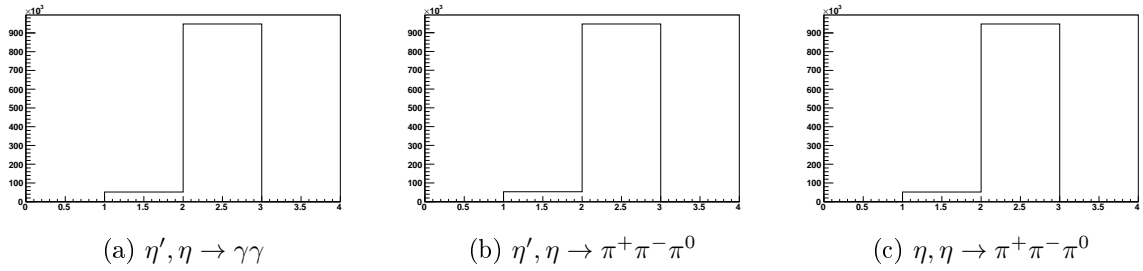


Figure 4.25.: Number of detected photons in the fast Monte Carlo simulation

4.6. Comparison With Data

A natural next step would be a comparison of the Monte Carlo results to real data, which can not be done in great detail, since it would be beyond the frame of this thesis. However an interesting observation in the 2008 η data should be briefly discussed here. The data is selected with the same cuts as described for the Monte Carlo simulation in section 4.4.1. If one looks at the transversal momentum of the η in the lab frame and plots $\mathbf{p}_x(\text{lab})$ of η vs. $\mathbf{p}_y(\text{lab})$ of η , with \mathbf{p} being the momentum 3-vector, one obtains Figure 4.26. The z -axis in the lab system (the direction of the beam) is pointing out of the $\mathbf{p}_x\mathbf{p}_y$ -plane towards the observer.

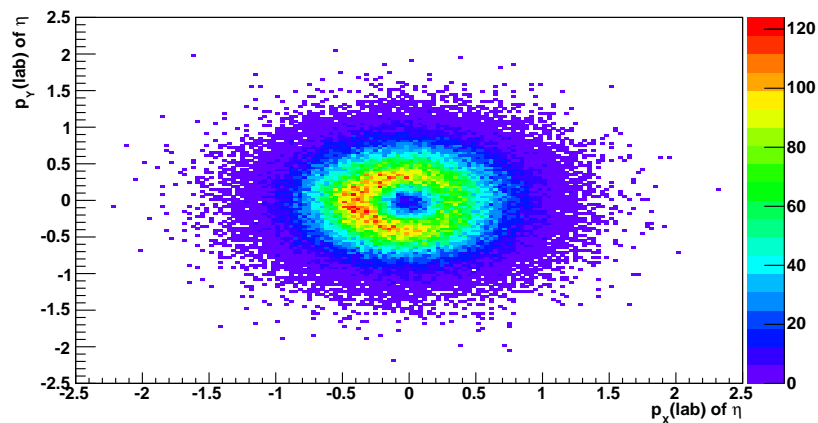


Figure 4.26.: $\mathbf{p}_x(\text{lab})$ of η vs. $\mathbf{p}_y(\text{lab})$ of η in real 2008 data

As you can see, there is a clear ring structure in the plot shown in Figure 4.26 with a global minimum at the center at zero transversal momentum of η . This ring can not be reproduced in the full Monte Carlo with and isotropic resonance decay at the first place, where the same $\mathbf{p}_x\mathbf{p}_y$ -distribution is plotted in Figure 4.27 for resonance masses not higher than 2GeV.

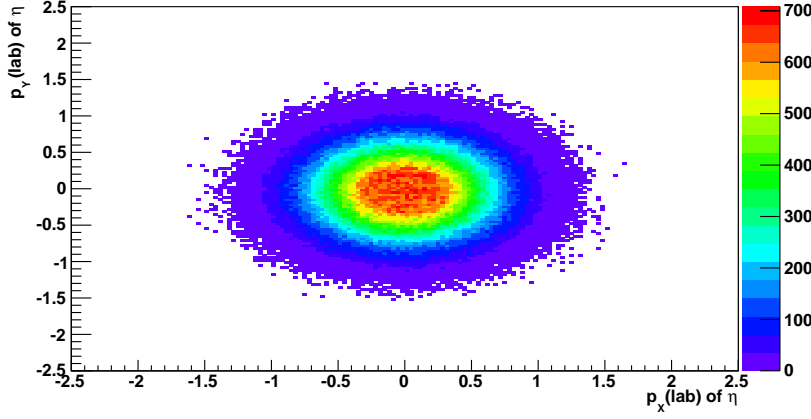


Figure 4.27.: $\mathbf{p}_x(lab)of\eta$ vs. $\mathbf{p}_y(lab)of\eta$ in full Monte Carlo simulation with $m_X < 2\text{GeV}$

However the ring structure appears also in the full Monte Carlo plot after introducing a weight of $\sin^2(\varphi_{GJ})$ on every bin entry, where φ_{GJ} is again the azimuthal angle of η in the Gottfried-Jackson frame of the resonance X . This simulates an anisotropic A_1 decay of X . Figure 4.28 shows again the $\mathbf{p}_x(lab)of\eta$ vs. $\mathbf{p}_y(lab)of\eta$ plot for the full Monte Carlo results, but this time weighted with this $\sin^2(\varphi_{GJ})$ term and the ring structure appears.

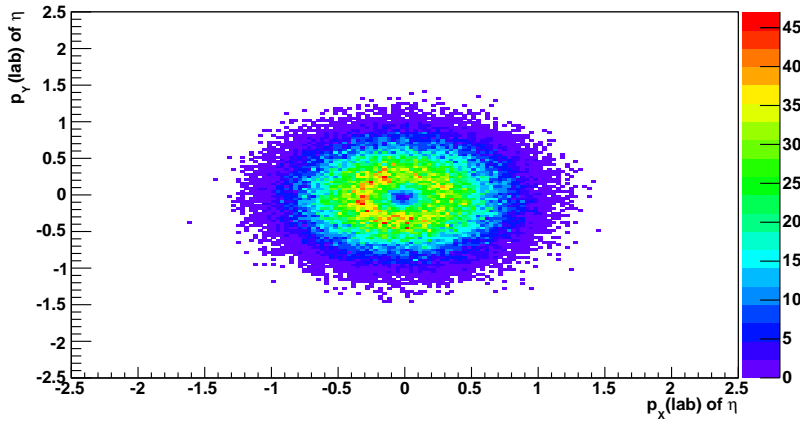


Figure 4.28.: $\mathbf{p}_x(lab)of\eta$ vs. $\mathbf{p}_y(lab)of\eta$ in full Monte Carlo simulation with $m_X < 2\text{GeV}$ and a weight of $\sin^2(\varphi_{GJ})$ on every bin

This ring is characteristic for diffractive excitation processes with an exchange of a

pomeron (see section 3.2.1). In strong interaction processes parity is conserved and one has a production plane, which makes it convenient to describe the amplitudes of the angular distribution in terms of reflectivity eigenstates $A_{\ell m}(\varphi, \theta)$, that are linear combinations of the spherical harmonics $Y_l^m(\varphi, \theta)$ as shown in Equation (4.7), with l and m as the angular and magnetic quantum numbers of the resonance X [21].

$$A_{\ell m}(\varphi_{GJ}, \theta_{GJ}) = \theta(m)[Y_l^m(\varphi_{GJ}, \theta_{GJ}) - \epsilon(-1)^m Y_l^{-m}(\varphi_{GJ}, \theta_{GJ})] \quad (4.7)$$

Here the introduced ϵ can take the values $+1$ or -1 and is called the reflectivity quantum number. Thus $0 \leq m \leq l$. For the detailed theoretical explanation I refer to [21] and [12]. Since diffractive meson production is dominated by pomeron exchange only $\epsilon = +1$ is expected and an the eigenstate looks like

$$A_{+1lm}(\varphi_{GJ}, \theta_{GJ}) = 2\theta_{GJ}(m)i \sin(m\varphi_{GJ}). \quad (4.8)$$

Hence the intensity $|A_{+1lm}(\varphi_{GJ}, \theta_{GJ})|^2$ is proportional to $\sin^2(\varphi_{GJ})$ in the case of $m = 1$.

$$|A_{+111}(\varphi_{GJ}, \theta_{GJ})|^2 \sim \sin^2(\varphi_{GJ}) \quad (4.9)$$

Thus the $\sin^2(\varphi_{GJ})$ dependency is a consequence of dominant positive reflectivity, which is a natural feature of diffractive excitation and is clearly visible in data through the appearance of the ring structure, which is also reproducible in the Monte Carlo simulation if the $m = 1$ case is taken into account by weighting with $\sin^2(\varphi_{GJ})$. The hole on the right side of the ring in Figure 4.26 (only visible in the colour version) can be identified with the hole in ECAL2, since a fast Monte Carlo simulation without an implemented hole shows a closed ring structure in the $\mathbf{p}_X \mathbf{p}_y$ plot of the η . The actual size of the break in the ring in Figure 4.26 is bigger than in the full Monte Carlo picture in Figure 4.27, which is due to dead detector cells near the hole in ECAL2 that lead to a bigger loss of events in the real data.

5. Conclusion And Outlook

As one main goal in the hadron program, COMPASS contributes to the search for exotic meson resonances. In general a partial wave analysis (PWA) is necessary to measure the exact quantum numbers of these resonant particle subsystems. To support such a PWA of the $\pi^-\eta'$ - and the $\pi^-\eta$ -system. One needs a good description of the acceptance of the detector responses. The focus of this thesis is a Monte Carlo simulation of the whole experiment, where those new resonances are produced in the $\pi^-\eta'$ and the $\pi^-\eta$ final states via diffractive excitation. After a realistic simulation of the full decay chains of the produced resonances, acceptance studies were performed with two Monte Carlo programs, a simple and fast photon acceptance Monte Carlo and a full Monte Carlo calculation with COMGEANT and CORAL.

The comparison of the fast photon acceptance Monte Carlo simulation, where only the ECALs and the RICH pipe geometry are taken into account, with the full COMGEANT and CORAL Monte Carlo chain shows that, despite the rather simple description of the experiment in the fast Monte Carlo, the acceptance as a function of many various variables is in agreement between the two simulations and thus can be understood quite well. Since charged particle detection is completely neglected in the photon acceptance Monte Carlo calculation the absolute value of the acceptance is consequently always larger but the flat shape of the efficiencies as functions of the generated resonance mass m_X , the momentum transmission t' , the Dalitz plots of η' and η , the azimuthal angle φ_{GJ} of the respective η' or η and the xy -distributions of the vertex position can be reproduced rather precisely.

The acceptance as a function of the polar angle θ_{GJ} in $\eta, \eta \rightarrow \pi^+\pi^-\pi^0$ decay channel is also of same shape in comparison. However in the η' case the efficiencies in the real and the photon acceptance Monte Carlo calculation are different and not in agreement with each other. The closer observation of secondary clusters in the real Monte Carlo simulation indicates that the effect of secondary charged particles, that is not implemented in the fast Monte Carlo, is not neglectable. A comparison with the acceptances in a fast Monte Carlo calculation without the RICH may indicate that the the RICH pipe is responsible for this effect. In this context a full Monte Carlo analysis of the η' channels without an implemented RICH tube would maybe illuminate the disagreement but is beyond the time schedule of this thesis. However a simple estimation of the RICH's influence on the photon acceptance, investigated with the fast Monte Carlo program, showed that the probability of a single photon hitting the RICH pipe, so that the event gets lost, is around 21% in the η channel in real data and the simulation.

The next step would be a more detailed comparison of the Monte Carlo results to real data. Therefore a precise implementation of dead detector cells would be crucial, since they may be responsible for different acceptance effects. Although this was not taken into account, a comparison of the full Monte Carlo calculation of the $\eta, \eta \rightarrow \pi^+ \pi^- \pi^0$ and real 2008 data of the same channel lead to an interesting observation. Before starting a partial wave analysis to obtain the quantum numbers of the resonant system, restrictions on the possible partial waves are already seen in the transversal momentum of the η . A global minimum at zero transversal momentum may be explained by the absence of resonances with magnetic quantum number $m = 0$, which is a general feature of diffractive excitation processes that can be pictured by pomeron exchange between the projectile pion and the target proton leading to natural reflectivity $\epsilon = +1$. In a $\mathbf{p}_x(lab)of\eta$ vs. $\mathbf{p}_y(lab)of\eta$ plot, one can see a $\sin^2(\varphi_{GJ})$ dependence with the bare eye, which tells that in the selected diffractive excitation processes there is only natural exchange referring to $m = 1$. This may already anticipate a selection of partial waves for the description of the resonant $\pi^- \eta'$ - or $\pi^- \eta$ -systems in a partial wave analysis.

A. Appendix

A.1. Software Versions

- ROOT: 5.28
- COMGEANT: current version (May 2011)
- CORAL: Slot3 Production CORAL
- PHAST: 7.073

A.2. Source Code

Here you find some source code parts that were used in this thesis. For the explanation see section 4.3.1. The following program parts were developed by Tobias Schlüter, Hauke Wöhrmann and me.

A.2.1. The Event Generator

```
//define particle masses in GeV
const double mP = .93827203;
const double mPi = .13957018;
const double mPi0 = .1349766;
const double mEta = .54775;
const double mEtaPr = .95778;

//uses random t distribution
//get Lorentz vectors in the CM frame
void diffEx(const TLorentzVector& lv1,
            const TLorentzVector& lv2,
            TLorentzVector& lv3,
            TLorentzVector& lv4,
            const double m3,
            const double m4)
{
    TLorentzVector W = lv1 + lv2;
    TVector3 boost = W.BoostVector();
```

```

TLorentzVector lv1CM = lv1;
lv1CM.Boost(-boost);

double s = W.M2();
double E3 = (s + m3*m3 - m4*m4) / (2.0*sqrt(s));
double E4 = (s + m4*m4 - m3*m3) / (2.0*sqrt(s));
double p3 = sqrt(E3*E3 - m3*m3);
double slope = 6.0;
double t, costh;
do
{
    t = -gRandom->Exp(1/slope);
    costh=(t + 2*lv1CM.E()*E3 - lv1CM.M()*lv1CM.M()
          - m3*m3)/(2*lv1CM.P()*p3);
}
while (TMath::Abs(costh) > 1. || -t < 0.1);
double theta = acos(costh);
double phi = gRandom->Uniform(-4*atan(1.0),4*atan(1.0));

lv3.SetXYZT( p3*cos(phi)*sin(theta),
             p3*sin(phi)*sin(theta),
             p3*costh,E3);
lv4.SetXYZT(-p3*cos(phi)*sin(theta),
            -p3*sin(phi)*sin(theta),
            -p3*costh,E4);

lv3.Boost(boost);
lv4.Boost(boost);
}

//Transforms Lorentz Vector into Gottfried-Jackson frame
TLorentzVector GJframe( TLorentzVector resX,
                        TLorentzVector Beam,
                        TLorentzVector lvGJ)
{
    TLorentzVector lvGJout = lvGJ;
    TRotation rotGJ;
    Beam.Boost(-resX.BoostVector());
    TLorentzVector Target(0.,0.,0.,mP);
    Target.Boost(-resX.BoostVector());
    lvGJout.Boost(-resX.BoostVector());
    rotGJ.SetZAxis(Beam.Vect(),-Target.Vect());

    return lvGJout.Transform(rotGJ.Inverse());
}

```

```

}

//get Lorentz vectors in the CM frame
void twobodydecay(const TLorentzVector& lv1,
                  TLorentzVector& lv2,
                  TLorentzVector& lv3,
                  const double m2,
                  const double m3)
{
    double s = lv1.M2();
    TVector3 boost = lv1.BoostVector();

    double E2 = (s + m2*m2 - m3*m3) / (2.0*sqrt(s));
    double E3 = (s + m3*m3 - m2*m2) / (2.0*sqrt(s));

    double p2 = sqrt(E2*E2 - m2*m2);
    double p3 = sqrt(E3*E3 - m3*m3);

    double costh = gRandom->Uniform(-1.0,1.0);
    double theta = acos(costh);
    double phi = gRandom->Uniform(-4*atan(1.0),4*atan(1.0));

    lv2.SetXYZT( p2*cos(phi)*sin(theta),
                 p2*sin(phi)*sin(theta),
                 p2*costh,E2);
    lv3.SetXYZT(-p3*cos(phi)*sin(theta),
                 -p3*sin(phi)*sin(theta),
                 -p3*costh,E3);

    lv2.Boost(boost);
    lv3.Boost(boost);
}

double PDW(double a, double b, double c)
{
    double sr = a*a + (b*b-c*c)*(b*b-c*c)/(a*a) - 2*(b*b+c*c);
    return 2*4*atan(1.)*sqrt(sr)/a;
}

void threebodydecay(const TLorentzVector& W,
                   TLorentzVector& lv1,
                   TLorentzVector& lv2,
                   TLorentzVector& lv3,
                   const double m1,

```

```

        const double m2,
        const double m3)
{
    double mmin = m1 + m2;
    double mmax = W.M() - m3;

    double wgtmax = PDW(W.M(), mmin, m3)*PDW(mmax, m1, m2);

    double m12, weight;
    int count = 0;
    do
    {
        count++;

        m12 = sqrt( gRandom->Uniform(mmin*mmin, mmax*mmax) );
        weight = PDW(m12, m1, m2) * PDW(W.M(), m12, m3);
    }
    while( weight < gRandom->Uniform(wgtmax) );

    TLorentzVector lv12;
    twobodydecay(W, lv12, lv3, m12, m3);
    twobodydecay(lv12, lv1, lv2, m1, m2);
}

double DalitzWeight (const TLorentzVector& W,
                    const TLorentzVector& lv1,
                    const TLorentzVector& lv2,
                    const TLorentzVector& lv3,
                    double* XY, double* abcd)
{
    TVector3 boost = W.BoostVector();
    TLorentzVector lv1W = lv1;
    TLorentzVector lv2W = lv2;
    TLorentzVector lv3W = lv3;
    lv1W.Boost(-boost);
    lv2W.Boost(-boost);
    lv3W.Boost(-boost);

    double T1 = lv1W.E() - lv1W.M();
    double T2 = lv2W.E() - lv2W.M();
    double T3 = lv3W.E() - lv3W.M();
    double Q = T1 + T2 + T3;

    double Xp = sqrt(3.) * (T2 - T3) / Q;

```



```

double Yp = ((lv1W.M()+2*lv2W.M())/lv2W.M()) * (T1/Q) - 1.;

XY[0]=Xp;
XY[1]=Yp;

double M2 = 1 + abcd[0] * XY[1] + abcd[1] * XY[1]*XY[1]
             + abcd[2] * XY[0] + abcd[3] * XY[0]*XY[0];

return M2;
}

////////////////////////////////////

//diffractive excitation , create resonance X
TLorentzVector X, pRec;
double mX = mPi + mEtaPr + gRandom->Uniform(3.0);
diffEx (beam, target ,X, pRec ,mX,mP);

//decay of resonance X
TLorentzVector Pim_X, Eta_X, EtaPr, Pip_EtaPr,
               Pim_EtaPr, Eta_EtaPr, Eta;
twobodydecay(X,Pim_X,EtaPr ,mPi,mEtaPr);

//decay of eta '
double M2etaPr, XYetaPr[2];
double abcdEtaPr[4] = {-0.127,-0.106,0.015,-0.082};
do
{
    threebodydecay(EtaPr,Pip_EtaPr,
                   Pim_EtaPr,Eta_EtaPr,mPi,mPi,mEta);
    M2etaPr = DalitzWeight(EtaPr,Eta_EtaPr,Pip_EtaPr,
                           Pim_EtaPr,XYetaPr,abcdEtaPr);
    gHist.Fill("hM2etaPr", "", 1000,0,3,M2etaPr);
}
while ( M2etaPr < gRandom->Uniform(1.1));

//Gottfried-Jackson frame
TLorentzVector Eta_XGJ = GJframe(X,beam,Eta_X);
TLorentzVector EtaPrGJ = GJframe(X,beam,EtaPr);

```

A.2.2. Photon Acceptance Monte Carlo Simulation

```

//define calorimeters
//ECAL1

```

```

const double e1xyz[3] = {-0.7,0.96,1399.5};//center of calorimeter
const double e1xr = 84.26 + 8*14.3;
const double e1yr = 10*14.3;
const double e1x[2] = {-e1xr + e1xyz[0] , e1xr + e1xyz[0]};
const double e1y[2] = {-e1yr + e1xyz[1] , e1yr + e1xyz[1]};
const double e1z[1] = {e1xyz[2]};
const double e1hx[2] = {-14*3.83+e1xyz[0],14*3.83+e1xyz[0]};//hole
const double e1hy[2] = {-8*3.83 + e1xyz[1] , 8*3.83 + e1xyz[1]};
//ECAL2
const double e2xyz[3] = {3.06,0.15,3325.2};
const double e2xr = 32*3.83;
const double e2yr = 24*3.83;
const double e2x[2] = {-e2xr + e2xyz[0] , e2xr + e2xyz[0]};
const double e2y[2] = {-e2yr,e2yr};
const double e2z[1] = {e2xyz[2]};
const double e2hx[2] = {2*3.83 + e2xyz[0] , 4*3.83 + e2xyz[0]};
const double e2hy[2] = {-3.83 + e2xyz[1] , 3.83 + e2xyz[1]};

//define RICH pipe
const double rpz = 748.7;
const double rprin = 4.985;
const double rprou = 5;
const double rplen = 314;
const double radlegFe = 1.76;

//gives integer 0,1,2 for hit calorimeter and position
int calohit(const TVector3& Vertex,
            const TLorentzVector& gamma,
            TVector3& CaloPosition)
{
    double x = gamma.X();
    double y = gamma.Y();
    double z = gamma.Z();

    if(z <= 0) return 0;

    // hit in ecal1 ?
    CaloPosition.SetX((x/z)*(e1z[0] - Vertex.Z()) + Vertex.X() );
    CaloPosition.SetY((y/z)*(e1z[0] - Vertex.Z()) + Vertex.Y() );
    CaloPosition.SetZ(e1z[0]);
    if(CaloPosition.X()<=e1x[0] || CaloPosition.X()>=e1x[1])
        return 0;
    if(CaloPosition.Y()<=e1y[0] || CaloPosition.Y()>=e1y[1])
        return 0;

```

```

if( CaloPosition.X()<e1hx[0] || CaloPosition.X()>e1hx[1])
    return 1;
if( CaloPosition.Y()<e1hy[0] || CaloPosition.Y()>e1hy[1])
    return 1;

// hit in ecal2 ?
CaloPosition.SetX((x/z)*(e2z[0] - Vertex.Z()) + Vertex.X() );
CaloPosition.SetY((y/z)*(e2z[0] - Vertex.Z()) + Vertex.Y() );
CaloPosition.SetZ(e2z[0]);
if( CaloPosition.X()<=e2x[0] || CaloPosition.X()>=e2x[1])
    return 0;
if( CaloPosition.Y()<=e2y[0] || CaloPosition.Y()>=e2y[1])
    return 0;

if( CaloPosition.X()<e2hx[0] || CaloPosition.X()>e2hx[1])
    return 2;
if( CaloPosition.Y()<e2hy[0] || CaloPosition.Y()>e2hy[1])
    return 2;

return 0;
}

//gives radiation lenghts of gammas
double hitRichPipe(TVector3& Vertex , TLorentzVector& gamma)
{
    const double d0 = rpz - (rplen/2.0);
    const double d1 = rpz + (rplen/2.0);

    // ( x )      ( Gx )      ( PVx )
    // ( y ) = lambda*( Gy ) + ( PVy )
    // ( z )      ( Gz )      ( PVz )

    double x = gamma.X();
    double y = gamma.Y();
    double z = gamma.Z();

    TVector3 fpos , bpos;
    fpos.SetXYZ( (x/z) * (d0 - Vertex.Z()) + Vertex.X() ,
                 (y/z) * (d0 - Vertex.Z()) + Vertex.Y() ,
                 d0);
    bpos.SetXYZ( (x/z) * (d1 - Vertex.Z()) + Vertex.X() ,
                 (y/z) * (d1 - Vertex.Z()) + Vertex.Y() ,
                 d1);

```

```

// (lambda*Gx + PVx)^2 + (lambda*Gy + PVy)^2 = r^2
const double a = x*x + y*y;
const double b = 2*(x*Vertex.X() + y*Vertex.Y());
const double cin=Vertex.X()*Vertex.X()+
                Vertex.Y()*Vertex.Y()-rprin*rprin;
const double cout=Vertex.X()*Vertex.X()+
                Vertex.Y()*Vertex.Y()-rprout*rprout;

const double lambdaIn = (-b + sqrt(b*b - 4*a*cin)) / (2*a);
const double lambdaOut = (-b + sqrt(b*b - 4*a*cout)) / (2*a);

const TVector3 In(lambdaIn*x + Vertex.X(),
                  lambdaIn*y + Vertex.Y(),
                  lambdaIn*z + Vertex.Z());
const TVector3 Out(lambdaOut*x + Vertex.X(),
                  lambdaOut*y + Vertex.Y(),
                  lambdaOut*z + Vertex.Z());

if(fpos.Perp() > rprout) return 0;

if(fpos.Perp() < rprin)
{
    if(bpos.Perp() < rprin) return 0;
    if(bpos.Perp() <= rprout) return (bpos-In).Mag()/radlegFe;
    else return (Out-In).Mag()/radlegFe;
}
else
{
    if(bpos.Perp() <= rprout) return (bpos-fpos).Mag()/radlegFe;
    else return (Out-fpos).Mag()/radlegFe;
}

return 0;
}

////////////////////////////////////

//gammas in calorimeters?
TVector3 g1_CaloPosition, g2_CaloPosition;
int c1 = calohit(vertex,g1,g1_CaloPosition);
int c2 = calohit(vertex,g2,g2_CaloPosition);

```

```
int a = 1; //1 = good (accepted) event

if(g1.E() < 1 || g2.E() < 1)
    a = 0;

if(c1 == 2 && g1.E() < 4)
    a = 0;

if(c2 == 2 && g2.E() < 4)
    a = 0;

if(c1 == 0 || c2 == 0)
    a = 0;

//gammas in RICH?
double len1, len2;
len1 = hitRichPipe(vertex, g1);
len2 = hitRichPipe(vertex, g2);

if(len1 > gRandom->Exp(9.0/7.0))
    a = 0;

if(len2 > gRandom->Exp(9.0/7.0))
    a = 0;
```


List of Figures

2.1. Photon-Gluon Fusion[20]	4
2.2. A Primakoff reaction[20]	5
2.3. $\pi^-\eta'$ mass distribution	6
2.4. COMPASS set up[2]	7
3.1. Nonet: pseudo-scalar mesons with $J^P = 0^-$ configuration, different charge Q , spin S , isospin I_3 , [22]	12
3.2. Decay scheme of the η' - and η -channel	14
3.3. Two-body scattering[15]	15
3.4. Pomeron exchange in diffractive excitation[10]	16
3.5. Two-body decay[15]	17
3.6. Three-body decay[15]	18
3.7. Dalitz plot[15]	19
4.1. generated Vertex distribution	23
4.2. Generated mass distribution ($\eta', \eta \rightarrow 2\gamma$)	23
4.3. Generated exponential t' distribution with a slope of 6	24
4.4. Generated angular distribution of the η'/η in the GJ-frame.	25
4.5. Generated Dalitz plots	26
4.6. ECALs in the photon acceptance Monte Carlo simulation	27
4.7. Position of photons in the ECALs	28
4.8. RICH pipe, $L = 314, 0\text{cm}$, $r = 4, 985\text{cm}$, $R = 5, 0\text{cm}$	29
4.9. X/X_0 of a photon hitting the RICH pipe	30
4.10. Position of photons in the ECALs with an implemented RICH	30
4.11. Radii of photons in ECAL2	31
4.12. Cutflow diagrams	34
4.13. z -distribution of the vertex position in the $\eta', \eta \rightarrow 2\gamma$ event class.	35
4.14. acceptance in z -distribution of the vertex position, red lines: Full Monte Carlo black lines: Fast Monte Carlo	36
4.15. Uniform acceptances in all simulated decay channels	36
4.16. Uniform acceptances in the photon acceptance Monte Carlo	37
4.17. Acceptance as function of $m(\pi^-\eta')$ or $m(\pi^-\eta)$, red lines: Full Monte Carlo black lines: Fast Monte Carlo	37
4.18. Acceptance as function of φ_{GJ} of η'/η	38
4.19. Acceptance as function of $\cos\theta_{GJ}$ of η'/η	38
4.20. Acceptance in m_X vs. $\cos\theta_{GJ}$	39
4.21. Acceptance in m_X vs. $\cos\theta_{GJ}$, fast MC without RICH pipe	40

4.22. Acceptance in $\cos\theta_{GJ}$, fast MC without RICH pipe	40
4.23. Number of reconstructed clusters in the ECALs	41
4.24. Number of good clusters in the ECALs	41
4.25. Number of detected photons in the fast Monte Carlo simulation	42
4.26. $\mathbf{p}_x(lab)of\eta$ vs. $\mathbf{p}_y(lab)of\eta$ in real 2008 data	42
4.27. $\mathbf{p}_x(lab)of\eta$ vs. $\mathbf{p}_y(lab)of\eta$ in full Monte Carlo simulation with $m_X < 2\text{GeV}$	43
4.28. $\mathbf{p}_x(lab)of\eta$ vs. $\mathbf{p}_y(lab)of\eta$ in full Monte Carlo simulation with $m_X <$ 2GeV and a weight of $\sin^2(\varphi_{GJ})$ on every bin	43

List of Tables

3.1. Different meson types and their quantum numbers	12
3.2. Final states of the decay channels	15
4.1. Used fit parameters for the Dalitz plots	25

Bibliography

- [1] AL., J. A. et: A measurement of the spin asymmetry and determination of the structure function g_1 in deep inelastic muon-proton scattering. In: *Phys. Lett. B* 206, 364 (1988)
- [2] AL., P. A. et: The COMPASS Experiment at CERN. In: *CERN-PH-EP/2007-001* (2007)
- [3] AL., P. L. A. et: Deep inelastic scattering of polarized electrons by polarized ^3He and the study of the neutron spin structure. In: *Phys. Rev. D* 54, 6620 (1996)
- [4] BELADIDZE, G.M. u. a.: Study of $\pi^- N \rightarrow \eta \pi^- N$ and $\pi^- N \rightarrow \eta' \pi^- N$ reactions at 37-GeV/c. In: *Phys. Lett.* B313 (1993), S. 276–282
- [5] BERGER, Christoph ; SPRINGER (Hrsg.): *Elementarteilchenphysik*. Springer, 2006
- [6] COLLABORATION, The C.: Proposal, The Common Muon Proton Apparatus for Structure and Spectroscopy. In: *CERN/SPSLC 96-14, SPSC/P 297* (1996)
- [7] COMGEANT: <http://www.jlab.org/gen/simul/>. WWW. 05/2011
- [8] CORAL: <http://coral.web.cern.ch/coral/>. WWW, Reference Guide. 01/2011
- [9] E852, Collaboration: Experimental Evidence for Hadronproduction of Exotic Mesons. In: *International Conference on Quark Nuclear Physics, Adelaide* (2000)
- [10] GRABMÜLLER, Stefanie: *Studies of Diffractive Particle Production at COMPASS*, Technische Universität München, Diplomarbeit, 2005
- [11] GRIFFITHS, David: *Introduction to Elementary Particles*. 1987
- [12] HADRON ANALYSIS GROUP, Tobias S. for the: *Partial Wave Analysis of 2008 $\eta' \pi^-$ data*. Talk, Analysis Meeting of the COMPASS Collaboration. 02.06.2011
- [13] KLEINKNECHT, Konrad ; TEUBNER, Wiesbaden .: (Hrsg.): *Detektoren für Teilchenstrahlung*. 4., überarb. Aufl., 2005
- [14] KOVARIK, Karol: Monte-Carlo Simulation of Three-Body Decays. In: *NA49 summer student* (2000)
- [15] (PARTICLE DATA GROUP), 075021 (. K. Nakamura et al.: *The Particle Data Group (PDG)*. <http://pdg.web.cern.ch/pdg/>. April 2011

- [16] PHAST: <http://ges.web.cern.ch/ges/phast/index.html>. WWW. 05/2011
- [17] ROOT: *User's Guide v5.26*. 05/2011
- [18] S. DONNACHIE, H. G. D. ; PRESS, Cambridge U. (Hrsg.): *Pomeron Physics and QCD*. 2002
- [19] SHEN, Chengping: Recent results from BESIII. In: *PoS HQL2010* (2010), S. 006.
– * Temporary entry *
- [20] WAGNER, Robert M.: *Commissioning of Silicon Detectors for the COMPASS Experiment at CERN*, Technische Universitat Munchen, Dissertation, 2001
- [21] WEITZEL, Quirin: *Precision Meson Spectroscopy: Diffractive Production at COMPASS and Development of a GEM-based TPC for PANDA*, Technische Universität München, Dissertation, 2008
- [22] WIKIPEDIA: *Mesons*. http://en.wikipedia.org/wiki/File:Meson_nonet_-_spin_0.svg. May 2011
- [23] WILLUTZKI, H.J.: EVIDENCE FOR EXOTIC MESON PRODUCTION IN π^-p INTERACTION AT 18GeV/c. In: *Brookhaven National Laboratory* (2000)
- [24] WÖHRMANN, Clemens Gregor H.: *Diffraktive Produktion von Drei-Körper-Endzuständen in π^-p -Wechselwirkung am COMPASS-Experiment (CERN)*, Ludwig-Maximilians-Universität München, Fakultät für Physik, Diplomarbeit, 2010

Danksagung

An dieser Stelle würde ich mich gerne bei allen bedanken, die es mir ermöglicht haben diese Arbeit zu schreiben und mir mit tatkräftiger Unterstützung zur Seite standen.

In erste Linie möchte ich Herrn Prof. Martin Faessler und Herrn Prof. Wolfgang Dünnweber dafür danken, dass mir von dieser Seite aus die Möglichkeit geboten wurde, die Bachelorarbeit in ihrer Arbeitsgruppe anzufertigen. Nicht nur bei den gemeinsamen Mittagessen konnte ich ständig auf neue Ideen, Blickwinkel und Ratschläge hoffen. Vielen Dank auch für die Ermöglichung des Aufenthalts am CERN, welcher tolle Einblicke in COMPASS gab und sehr interessant und motivierend war.

Herzlichst möchte ich auch Hauke Wöhrmann danken, der mir einen schnellen Einstieg in die Materie und die Arbeitsmethoden bereitet hat und dem ich alles Gute für seine Doktorarbeit wünsche.

Mein besonderer Dank gilt Tobias Schlüter, der mir auf sehr interessante und spannende Weise das Experiment näher brachte und von dem ich auf etlichen Gebieten wahnsinnig viel lernen konnte.

Erklärung

Ich erkläre hiermit, dass ich die vorliegende Bachelorarbeit selbständig und nur unter Verwendung der angegebenen Literatur und Hilfsmittel angefertigt habe.

Ort und Datum:

.....
(Unterschrift des Studenten)